



UNIVERSITAT POLITÈCNICA  
DE CATALUNYA



# MASTER THESIS

## DEVELOPMENT OF AN OBJECT ORIENTED THUNDERSTORM NOWCASTING SYSTEM FOR BARCELONA AIRPORT

Núria Devanthéry Arasa

### **SUPERVISED BY**

Dr. David Pino González  
Dr. Monika Pfeifer

**Universitat Politècnica de Catalunya**  
**Master in Aerospace Science & Technology**  
March 2010



# **Development of an Object Oriented Thunderstorm Nowcasting System for Barcelona Airport**

BY

Núria Devanthery Arasa

DIPLOMA THESIS FOR DEGREE

Master in Aerospace Science and Technology

AT

Universitat Politècnica de Catalunya

SUPERVISED BY:

Dr. David Pino González  
Department of Applied Physics

Dr. Monika Pfeifer  
HYDS Research Department



## **ABSTRACT**

Weather is the main source of problems in air traffic, mostly at the airport area during the phases of landing and takeoff. Especially, thunderstorms are the principal reason for flight delays and one of the main threats on air safety. A thunderstorm information system at near real time providing information about the location and intensity of the thunderstorms near the airport would allow tactical decisions at the airport area that would help to reduce the impact on air safety and flight delays.

The goal of this master thesis is to develop a thunderstorm information system for Barcelona airport. The purpose of the system is to provide information about all the thunderstorms that are near the airport area or approach it, including its location, horizontal extension, velocity and intensity. The system will generate alarms for the thunderstorms that are forecasted to enter the airport area.

The alarm system is based on radar observation of the Catalanian radar network. Thunderstorms are defined as regions with reflectivity exceeding a threshold, and short-term forecasts are done applying a nowcasting algorithm based on extrapolation of the observations.

The thunderstorm oriented alarm system developed within this master thesis has been applied to several case studies and the forecasting skill of the system has been evaluated against observations, providing reliability in time up to 30 minutes.



# CONTENTS

<b>1. INTRODUCTION .....</b>	<b>1</b>
<b>2. THEORETICAL BACKGROUND.....</b>	<b>3</b>
2.1. PHYSICS OF THUNDERSTORMS .....	3
2.1.1. Thunderstorm Development .....	3
2.1.2. Different Forms of Thunderstorms.....	6
2.2. OBSERVATION OF THUNDERSTORMS BY RADAR .....	7
2.2.1. Radar Principle .....	7
2.2.2. Meteorological Targets .....	8
2.2.3. Radars Products .....	9
2.2.4. Data Quality: Errors .....	10
2.3. SHORT TERM FORECASTING OF THUNDERSTORMS .....	11
2.3.1. Area Tracking Techniques.....	11
2.3.2. Cell Centroid Techniques .....	13
2.3.3. Operational Nowcasting Techniques .....	14
<b>3. METHODOLOGY .....</b>	<b>16</b>
3.1. DATA .....	16
3.2. MAIN BLOCKS OF THE ALARM SYSTEM DEVELOPMENT .....	18
3.2.1. Storm Detection .....	18
3.2.2. Storm Tracking and History Derivation .....	19
3.2.2.1 Storm Tracking .....	19
3.2.2.2. Storm Attributes and History Derivation.....	21
3.2.2.3. Mergers and Splits.....	23
3.2.3. Nowcasting .....	23
3.2.4. Alarm Generation.....	26
3.2.5. Evaluation of the System .....	26
<b>4. RESULTS.....</b>	<b>29</b>
4.1. CASE1: 25 JUNE 2009.....	29
4.2. CASE 2: 15 OCTOBER 2005 .....	37
4.3. CASE 3: 13 SEPTEMBER 2006.....	44
<b>5. CONCLUSIONS .....</b>	<b>51</b>
<b>REFERENCES .....</b>	<b>54</b>



# 1. INTRODUCTION

Adverse meteorological conditions are the main source of problems on airport areas.

Weather is the main cause of flight delays and the main source of security problems on airport areas. Specially, thunderstorms are known to be the usual main source of delay problems in aircrafts in the airport, mainly during landing and take off (approximately the 50% of the serious delays (Weber et al., 1993)).

In general, when flights can be grouped along standard routes, air traffic controllers can manage the flow efficiency and meet the scheduled demand. But when flights deviate from the standard routes they must interact actively with the aircraft, so each controller can handle fewer aircrafts (Evans et al., 1994). That means an increase of the delays. This problem takes importance if we think that the air traffic is going to increase in the next 20 years.

Every day, strategic air traffic decisions have to be taken by the traffic management controllers usually with the help of two-to-six hours forecast. But when we are in a convective scenario another kind of system with a shorter lead time (the time of life of a convective cell is usually no longer than 20-30 minutes) would be extremely useful. Due to their short life time, convective cells are difficult to forecast for long periods of time. More precisely, the accuracy of these forecasts generally decreases very rapidly during the first 30 minutes (Wilson et al., 1998). Because of this, short term forecasting techniques play a very important role here.

A correct knowledge of the weather state could help to reduce the time of delays, and could help the airport management to take tactical decisions of maneuvering in a short period of time that can increase the security and the efficiency of the flights.

In this Master Thesis, an information system oriented to thunderstorms applied to Barcelona airport area is proposed. This system will provide information at real time about the thunderstorms that are approaching the airport area with the attributes that are defining them and have some interest for the aviation, for example, the propagation velocity, its maximum reflectivity and its horizontal extension. This system will have to provide the information in a manner that its interpretation will require no meteorological interpretation.

This real time support information system would make possible to improve the safety of air travel in adverse weather conditions by means of making possible a better planning support.

In order to develop the proposed system, thunderstorms will be detected using near-real time radar data of observations of the Catalonian radar network. Thunderstorms will be defined as areas exceeding a given reflectivity threshold (35 dBZ). The detected convective cells will be tracked by means of the overlap between the extrapolation of the cells of a certain time image  $t$  and the observed cells at the consecutive in time image  $t+1$ . The extrapolation will be based on the motion field derived from the maximum correlation pattern of the two consecutive last radar images. The convective cells that have maximum overlap with the extrapolated ones are going to be identified as the same thunderstorm, so they are going to inherit its history. The history will consist in the features of the cell since its detection to the time of the last observation. These features are the position of the centroid, the area trend, the maximum intensity of the thunderstorm cell and the velocity and direction of the cell centroid. Then, the forecast is going to be done applying a nowcasting algorithm (Berenguer et al., 2008) to provide short-term forecasts based on the extrapolation of the observations. The last step of the alarm system is the generation of an algorithm that automatically will generate alarms when a forecasted thunderstorm cell hits the airport area.

The verification of the system performance will be done in basis of the commonly used statistical skill scores Probability of Detection, False Alarm Ratio and Critical Success Index. Due to the difficulty of providing a significative statistical verification with only the airport area corresponding to the Barcelona airport, 100 hypothetical airports are going to be invented over Catalonia in order to do the verification.

Three cases (each case consisting in 24 hours of study) are going to be analyzed in detail, in order to demonstrate and evaluate the developed thunderstorm nowcasting system.

## 2. THEORETICAL BACKGROUND

Thunderstorms have major impact on aviation, especially during the most critical flight phases: take off and landing. Moreover, they reduce both terminal and en route airspace capacity. So, as said before, the objective of this work is to identify and forecast thunderstorms at the airport area, in order to have a better management of the terminal routes that can allow a reduction of flight delays and an improvement of air security.

In order to do so, basic knowledge in the following fields is needed: thunderstorm physics to understand the phenomenon, its life cycle and why it is difficult to forecast them, radar meteorology because the system will be based on radar observations, and short term forecasting techniques because they are the methods used to forecast thunderstorms and for which some previous works had been taken into account to develop the thunderstorm nowcasting system exposed in this work.

### 2.1. Physics of Thunderstorms

Thunderstorms are one of the most impressive meteorological phenomena due to their potentially dangerous features.

During their life cycle, thunderstorms develop a number of features that are dangerous to aviation: turbulence resulting from strong updrafts cores on the relatively young cells, damaging lightning, large hailstones, tornadoes and intense precipitation. These features are hazardous to aircraft because of its intense turbulence and because it can also reduce visibility, create icing situations, and affect landing and take off performance of an aircraft. For example, if an aircraft enters a thunderstorm, the aircraft could experience updrafts and downdrafts that exceed 3,000 feet per minute.

These phenomena develop rapidly due to the typical short life cycle of convective cells, which makes especially difficult to forecast thunderstorms for long lead times.

In order to understand so, the general development of a thunderstorm and the different forms in which they usually present are detailed below.

#### 2.1.1. Thunderstorm Development

In order to forecast thunderstorms, its typical life cycle has to be understood.

For the formation of thunderstorms, three ingredients are needed: moisture, atmospheric instability, and usually an additional lifting mechanism.

If the atmosphere is unstable, the environment temperature decreases very rapidly with height ( $|dT/dz| > 9.8 \text{ K/km}$  in non saturated conditions, see Stull 2000 for an explanation). In these conditions vertical movements are enhanced and the air near the ground can easily move upwards because it has more buoyancy than the surroundings. During its ascent, it can be demonstrated that the temperature of this air parcel decreases  $9.8 \text{ K/km}$ . The air parcel will keep on moving upwards until a stable layer is found, where the buoyancy of the air parcel would be lower than the environment.

During this ascent, the water vapour of the parcel remains approximately constant. If the parcel temperature decreases enough, the saturation point (condensation) can be reached and a cumulus cloud appears. The temperature at which condensation starts is called dew point temperature. When the vapour condenses to form liquid water, the latent heat (energy stored from the evaporation of liquid water) is released back into the environment. Consequently, the buoyancy of the air parcel is enhanced and the cumulus cloud can grow even more. From this point, in order to form a cumulonimbus cloud an additional lifting mechanism is needed. Typical lifting mechanisms are: differential heating, which is due to the different rate of heating of the ground and the low atmosphere, fronts, that are defined as the boundary between two air masses of different temperature (and other properties, e.g. humidity) so they make warm moist air to lift, and orographic forcing by the overflow of mountains.

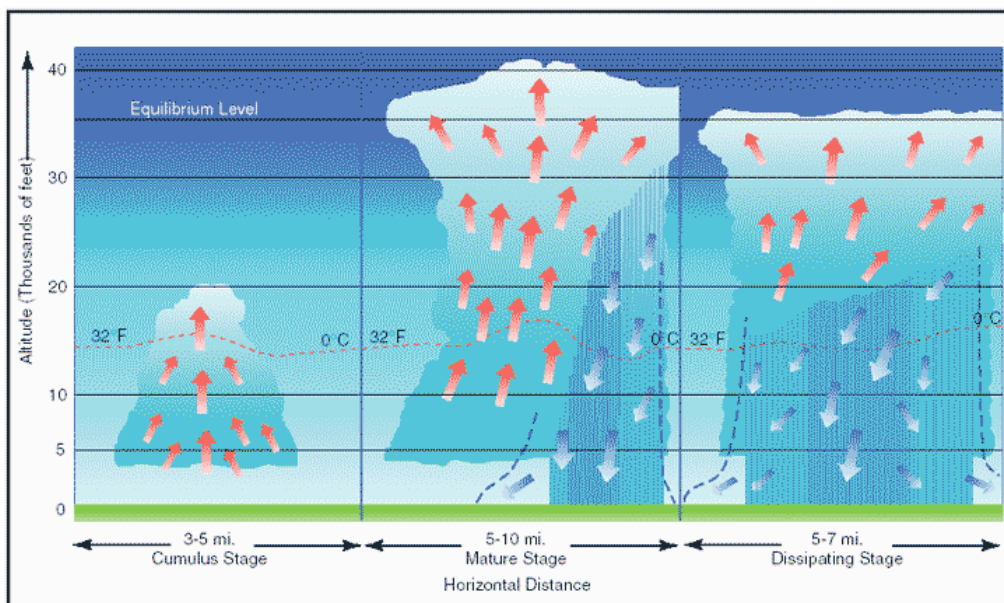


**Figure 1. Thunderstorm stage scheme. The figure shows the three main stages of the life of a thunderstorm: (1) cumulus stage, (2) mature stage and (3) dissipating stage. Duration of each stage is written in the horizontal axis. Red arrows represent warm air movements and blue arrows cold air directions. (Source: [www.free-online-private-pilot-ground-school.com](http://www.free-online-private-pilot-ground-school.com)).**

Cumulonimbus clouds continues growing as long as warm air below continues to rise, leading to the mature stage of a thunderstorm (see second part of Figure 1). The cumulonimbus will grow until an absolutely stable layer is found. This fact usually occurs at the tropopause.

If the water cloud drops, due to strong updrafts, reach extremely cold areas in the atmosphere, ice is produced. Into the cloud, particles grow generally by two mechanisms: by collision or coalescence between water and ice drops, and by differences in vapour pressure between ice crystals and supercooled water that makes the ice crystals to absorb the water vapour that was on the water droplets. Ice crystals or water drops start to fall through the cloud when the updrafts can no longer hold them up. Meanwhile, cool dry air starts to enter the cloud. Because cool air is heavier than warm air, it starts to descend in the cloud (known as a downdraft). The downdraft pulls the heavy water downward, making rain.

Figure 2 shows a vertical cross section through a mature cumulonimbus with the corresponding vertical movements. It can be observed how the lift of warm air (red arrows) enhances the downdrafts of cold air (blue and purple arrows). It can be seen how they get progressively colder with height (pink arrows), and how they sink due to the increase of density and become cold downdrafts.

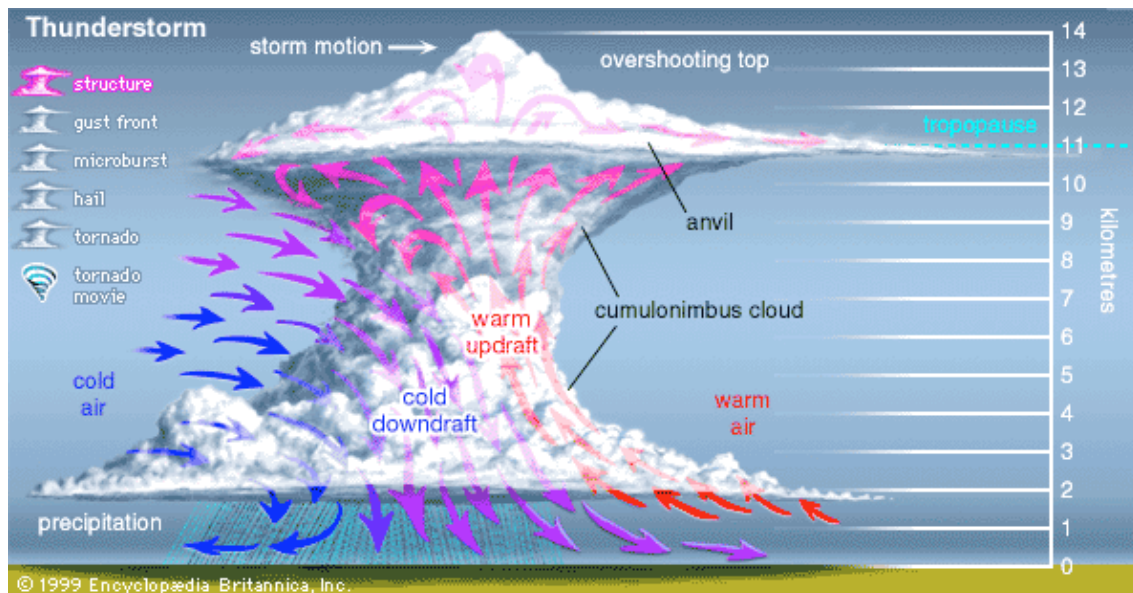


**Figure 2. General structure common in all cumulonimbus clouds (Source: Encyclopædia Britannica)**

Lightning activity is associated to thunderstorms in their mature stage. Lightning results from the separation of charges due to the collisions between particles into the cloud. These charges are then separated to larger distances by the updrafts and downdrafts present inside the cloud. When the potential difference is large enough, intracloud lightning or cloud to ground lightning takes place.

During the mature stage of the cloud, strong damaging winds, for example wind shear, occur. Air currents due to downdrafts of cool air are generated when rain-cooled, denser air sinks inside a thunderstorm. Evaporative cooling intensifies downdrafts, as drier air from the edges of the storm mixes with moist air within the storm. These movements of air, called microbursts, can be seen in Figure 2.

The previous processes lead to a rapid downward rush of air. As the air impacts the ground it is forced to spread out laterally causing wind gusts, associated with thunderstorms (see Figure 3 for a scheme of the vertical air movements causing wind gusts). Wind gusts are especially dangerous to aircraft landing. When encountered close to the ground, these excessive downdrafts and rapid changes in wind direction can produce a situation in which it is difficult to control the aircraft.

Once the vertical motion near the top of the cloud slows down near the tropopause, the top of the cloud spreads out and takes on an anvil-like shape (see anvil part on Figure 2).

As precipitation develops throughout the cloud, the downdraft circulation gradually becomes more extensive until, in the dissipating stage (see third part of Figure 1), when most of the energy has dissipated because of precipitation, it occupies the entire cloud. At this point, downdrafts replace the updrafts needed to sustain the storm, so droplets can no longer grow and precipitation soon ceases.

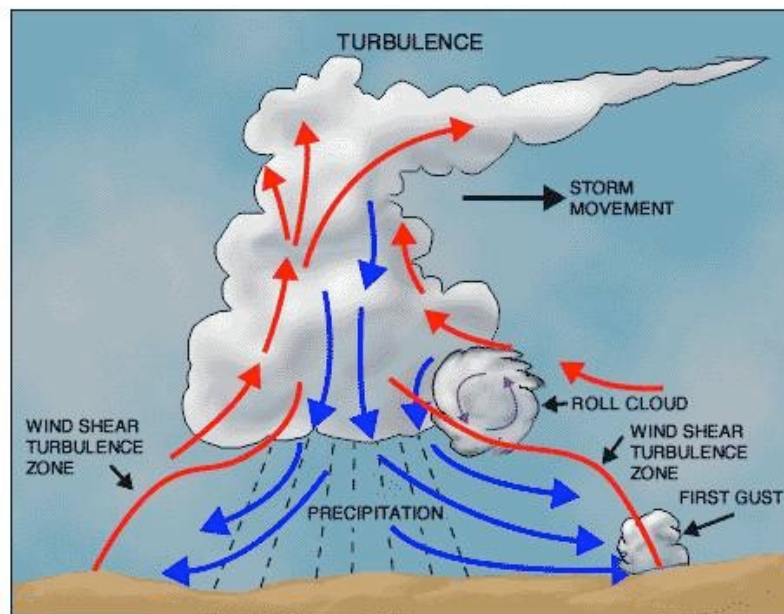


Figure 3. Thunderstorm Gust Front (Source:<http://quest.arc.nasa.gov/aero/virtual/demo/weather/tutorial/tutorial5c.html>)

### 2.1.2. Different Forms of Thunderstorms

The most common form of thunderstorms in Europe is as single individual cells (the mechanism of their formation has been explained in previous section). Less frequently, multicell thunderstorms occur. They consist on several individual cells that are in different stage of development. Contrarily to individual cells, their life time can last several hours.

By the other side, thunderstorms triggered by a cold front tend to form along the cold front line. Their movements are then, similar to the movement of the front.

## 2.2. Observation of Thunderstorms by Radar

Thunderstorms are usually observed by satellites, lightning detection systems and weather radars.

Radar is the most effective instrument to obtain observations in cloud systems on convective scales because it provides 3-D information with high spatial and temporal resolution, and large coverage. It provides useful information to understand cloud physics and dynamics, with special utility on measuring the falling precipitation. The precipitation is measured by means of an indirect measure, the reflectivity of the atmospheric targets.

### 2.2.1. Radar Principle

Radars operate transmitting an electromagnetic wave into the atmosphere that is reflected by the precipitation and is received back to the radar antenna (see Figure 4).

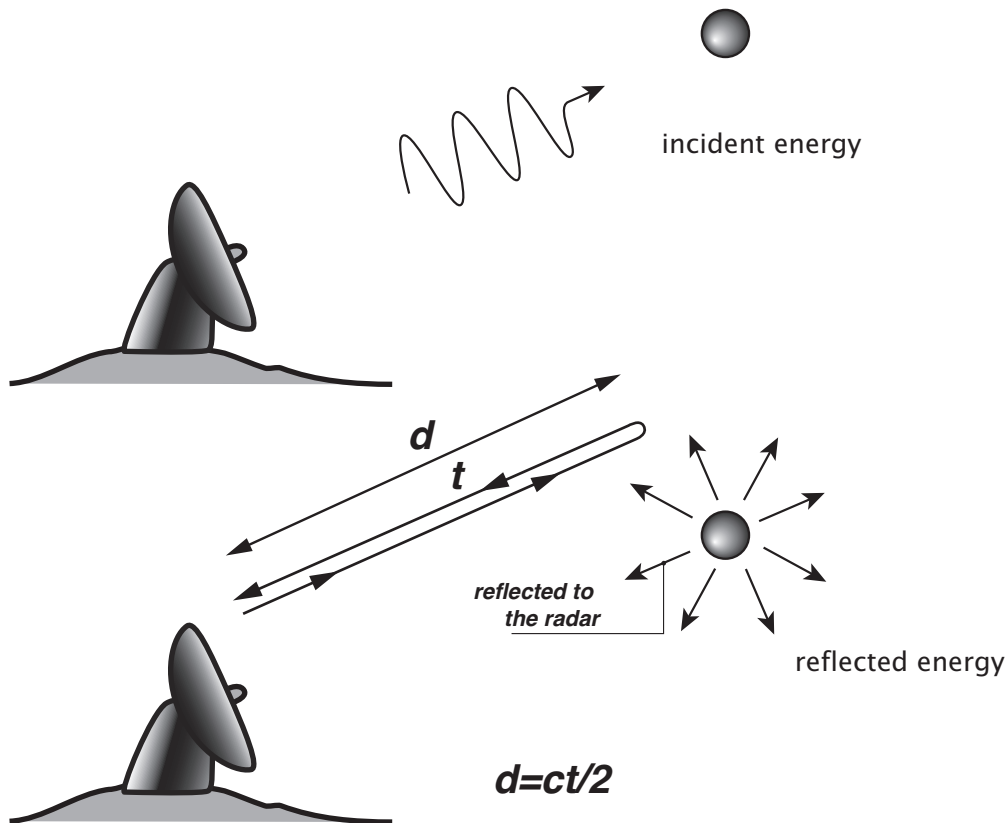


**Figure 4. Radar principle.** Radar operates transmitting an electromagnetic wave in the atmosphere that is partially reflected back. (Source: Sánchez-Diezma, 2001)

The data important to process in relation to thunderstorm observations is distance (or range), reflectivity ( $Z$ ) and radial velocity ( $V_r$ ).

The distance of the target is computed by means of the time between the emitted and the received signal, which travels at the speed of light,  $c$ . Figure 4 shows how the electromagnetic wave is reflected by the target and how its distance is computed.

Reflectivity is obtained from the returned power. Precipitation particles (rain, snow, graupel, hail) detected by meteorological radars are called targets. The returned power depends on the number of drops per unit volume, their sizes, their physical state (ice, water, etc) and the shape of the individual elements of the group.

Doppler radars measure the radial velocity component of the velocity of the targets ( $V_r$ ) using the Doppler effect. So, measuring the phase shift between two observations at different times, it is possible to obtain the moving velocity of the measured object in the direction object-radar (radial component).

### 2.2.2. Meteorological Targets

The measurement of the amount of precipitation that is reaching the ground is the most important quantitative use of radar. There exists an empirical relationship between radar reflectivity and rainrate, given by:

$$Z=aR^b$$

where  $Z$  ( $\text{mm}^6 \text{ m}^{-3}$ ) is the reflectivity factor and  $R$  ( $\text{mm h}^{-1}$ ) is the rainfall rate, and  $a$  and  $b$  are empirical constants. Due to the large variability of  $Z$  it is expressed in logarithmic scale:  $dBZ = 10\log_{10}(Z)$

Several experimental works obtained the values for relation Z-R. The most commonly used is the Marshall and Palmer relationship (Marshall et al., 1948):

$$Z = 200R^{1.6}$$

The detection of snow is more difficult than the detection of rain. This is because snow has a smaller dielectric constant, which reduces the backscattered signal considerably. Furthermore, precipitation rates for snow tend to be smaller than for rain, and usually snow storms are lower (in altitude) than rain storms (the lower the precipitation is, the less detectable at large distances by the radar because it would be below the radar beam).

The radar reflectivity range usually goes from approximately 10 dBz to 50 dBz for precipitation. In storms, reflectivity measures can be as high as 75 dBZ, where reflectivity measures higher than 55 dBZ are associated to hail.

Hail is defined as precipitation in the form of ice that has a diameter of at least 5 mm. The reflectivity from hail depends upon whether the outside surface is wet or dry or if there is any water enclosed in the hail, which changes the dielectric constant and hence the backscatter characteristics. Dry hail has a lower reflectivity than wet hail of the same size. Moreover, reflectivity from hailstones can change as they fall from above the melting level to the ground below the melting level.

On the other side, clouds are not detected by radars, because they are made of small water droplets and ice crystals that produce a contribution to reflectivity generally negligible. Usually only precipitating clouds produce detectable echoes. This is the reason why the initiation phase of a thunderstorm is not detectable by radar observations.

Interpretation of the radar reflectivity scale		
Type and intensity		Reflectivity
Drizzle or clear air targets (bugs, etc.)		0 dBZ
Very light rain or snow	A few raindrops or snowflakes	10 dBZ
Light rain or snow	Typical of spring/fall: 1-2 mm/hr	25 dBZ
Moderate precipitation	Strong for spring/fall: 5 mm/hr	35 dBZ
Heavy rain	Summer showers: 20 mm/hr	45 dBZ
Very heavy rain or hail	Peak of thunderstorms: 100 mm/hr	55 dBZ

**Table 1.** The table shows the mean reflectivity values for some meteorological phenomena or targets (Source: [http://www.radar.mcgill.ca/mcgill\\_img.html](http://www.radar.mcgill.ca/mcgill_img.html)).

### 2.2.3. Radars Products

There exist several ways to display radar data taking into account the observing principle.

Radars scan the atmosphere for several elevation angles (angle between the antenna and the horizontal). For each of them, the antenna makes a continuous (because the time between emission and reception is negligible) rotation movement of  $360^\circ$ , so the final result is a semi-spherical volume of information.

Usually, radar products generated from this type of observation are displays of the radar data in a map-like format, so they give all the information related to the position that is required by meteorological purposes.

PPI (Plan Position Indicator) provides information of the reflectivity of a determined elevation. The return is then mapped on a horizontal plane with the radar site at the centre of the display. Range is the distance from it, and concentric circles represent height above ground (see Figure 5).

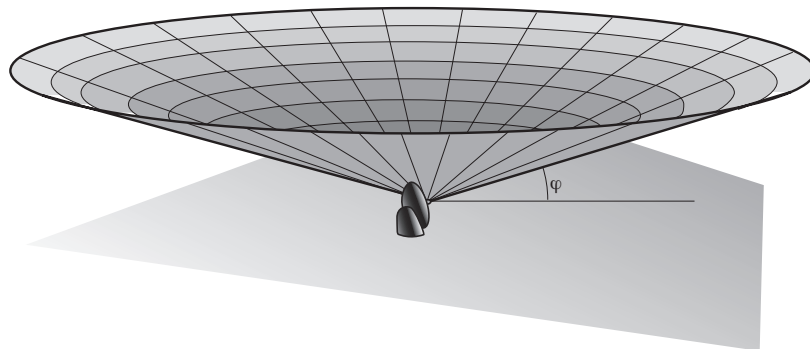


**Figure 5.** Volume scanned by a radar at elevation angle  $\varphi$  (Source: Sánchez-Diezma, 2001)

The interpretation of PPI's can be difficult because the height of the beam in the atmosphere is not constant. With increasing distance, the observations come from higher altitudes. This has to be taken into account when interpreting a PPI.

Another problem related to PPI is the ground echo found near the radar from orographic obstacles that intersect and block the radar beam.

CAPPIs (Constant Altitude Plan Position Indicator) are composed from the information from different PPI's representing only observations at a fixed altitude. The scheme of the PPI parts used to form the CAPPI image is shown in Figure 6.

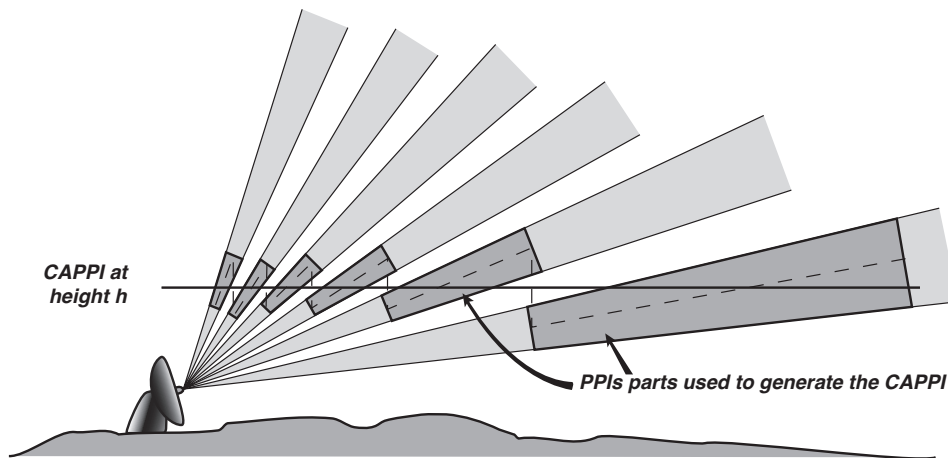


**Figure 6. CAPPI construction scheme. (Source: Sánchez-Diezma, 2001)**

Using the data at the right distance, it is possible to form an annular ring of data at a certain height. The CAPPI is obtained assembling all the rings coming from different angles.

With the use of CAPPI images, some of the problems related to PPI images are solved, as for example the problems related with change in altitude with distance to the radar and the ground echoes problems that are found near the radar. However, there exist some disadvantages, as the loss of resolution due to the manipulation of the PPI images.

A RHI (Range-Height Indicator) scan is a vertical cross section through a storm. The horizontal axis is the distance from radar and the vertical axis is the height above it. This kind of display is kind of complementary with PPI images.

#### **2.2.4. Data Quality: Errors**

Due to the observing principle, radar observations have associated a number of different errors. These errors must be known for the interpretation of radar observations. The most important are ground clutter, attenuation, bright band and errors due to the increase of altitude and size of the beam. However, even taking into account the different error sources, radar observations are the best available information on precipitation in the atmosphere.

Ground clutter error is related to echoes from ground targets, for example mountains. It can attenuate or hide echoes of targets located behind the ground target. Moreover, it returns a false echo. A similar source of false echoes corresponds to echoes due to non-meteorological moving objects, for example birds or aircrafts.

The increase of altitude and size of the beam with distance to the radar means a loss of resolution due to the beam volume.

Attenuation is also important because it produces a loss of energy on the radar beam due to the absorption and dispersion of this energy on the drops.

Another phenomenon to take into account is the bright band. The bright band is an area with high reflectivity due to the transition of the ice and snow to water (melting point) at the 0° C area. It is produced because of the different reflectivity of ice and water particles (the reflectivity for snow particles is lower than for rain particles) and their different terminal velocity (usually snow drops fall slowly than rain drops, so the concentration of rain particles decrease when snow melts, and thus the reflectivity below the melting level decrease). The bright band phenomenon has to be taken into account in order to not mistake it for hail or high reflectivity storms.

A last source of error is due to the relationship Z-R used. The incorrect use of one of them depending on the phenomenon measured can lead to an erroneous estimation of the precipitation.

## **2.3. Short Term Forecasting of Thunderstorms**

Due to the very short and rapid life cycle, the best forecasts of thunderstorms are based on the extrapolation of observations (mainly based on radar or satellite) at near real time. Extrapolation techniques are part of the group of techniques called nowcasting.

Usually, nowcasting range of forecasts goes from 0 to 2 or 3 hours. Nowcasting techniques have an accuracy that decays very fast during the first 30 minutes of forecast for individual convective cells due to the short lifetime of this kind of cells. For more organized features the forecast time can be 2 hours or more.

In the nowcasting techniques based on extrapolation, individual cells are detected from observations, tracked, and then their future position is extrapolated based on past observation information (mainly with some form of extrapolation of the movement on the features data).

Depending on the features used to make the extrapolation, these techniques can be classified in cell trackers, if they treat convective cells as an individual identity, or area trackers, if they use the whole image to find patterns between two consecutive images in time.

Historically, the extrapolation of convective cells has been associated to cell centroid techniques, but the derivation and use of motion fields has the advantage that it can be used directly in the extrapolation to determine variation in echo size or in other features related to radar contours.

### **2.3.1. Area Tracking Techniques**

Area tracking techniques use all the image in order to find patterns between two consecutive images. These techniques partition the images in boxes and for each box on the first image, they look for the most similar box on the second image. The generated vectors are the estimated movement vectors, used posteriorly to extrapolate the features of the second image.

Area tracking techniques use methods as pattern recognition and cross-correlation technique to find patterns between two observed fields. Pattern recognition (Austin, 1985), consists on the use of similarities between two data fields at successive times. On the other side, the cross-correlation technique (Rinehart et al., 1978; Tuttle et al., 1990) partitions the data fields into blocks or features, and identifies the movement vector that maximizes the correlation between a feature in the latest data field and the corresponding, but translated, feature in the previous data field. Figure 7 shows a scheme of TREC (Tracking Radar Echoes by Correlation) method, developed by Rinehart and Garvey. It can be observed that, in order to identify the movement vector, a searching range is defined around each box. The range is calculated depending on an estimated maximum velocity and the time between images. Other area trackers work very similar (Mecklenburg et al., 2002).

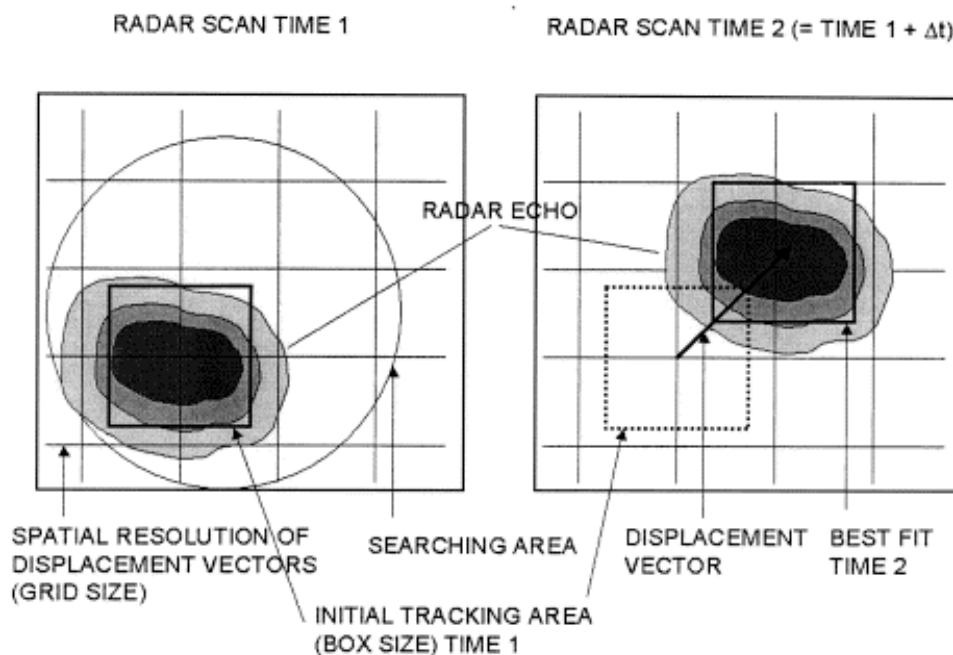


**Figure 7. Concept of the TREC (Rinehart et al., 1978) area tracking algorithm.**

Afterwards, COTREC (COntinuity of TREC vectors; Li et al., 1995) was developed to apply a continuity constraint on the TREC vectors. This method was developed as an extension to TREC, in order to smooth its velocity field by replacing vectors that deviates more than  $25^\circ$  from the mean direction of its neighbours and with zero velocity by an average of its neighbours (Li et al., 1995). Moreover, it applies a variational technique to the vectors in order to apply the continuity constraint.

### 2.3.2. Cell Centroid Techniques

Cross-correlation techniques were followed by storm cell centroid identification and tracking techniques. Wilk et al., 1970, developed a centroid identification technique based on 2D radar data to find storm motion and precipitation estimations by means of tracking and extrapolating the cell centroid. The technique identified cells as regions of echo above a defined reflectivity threshold where an intensity-weighted centroid was computed for each one of the regions. Afterwards, some variations on the technique were applied by Zittel, 1976, and others, in order to improve it.

Bjerkaas et al., 1979, developed and tested a centroid tracking algorithm that became the basis for a serie of algorithms used to show echo motion in convective cells.

Duda et al., 1972, refined these techniques in an attempt to handle echo merging and splitting. Dixon et al., 1993, made use of geometric algorithms in order to detect storm merging and splitting based on the anterior technique. They developed a system for tracking cells and estimating its attributes based on the cell past trends. An example of the output from this algorithm is TITAN (Thunderstorm Identification Tracking Analysis and Nowcasting).

In TITAN, storms are modelled as ellipses. Storms are matched using a real overlap between observations at two successive observations. If storm shapes at two successive times overlap significantly, these shapes are supposed to be from the same storm. Then, a centroid optimization scheme determines the most likely match between storms identified at successive scans. The scheme is represented in Figure 8.

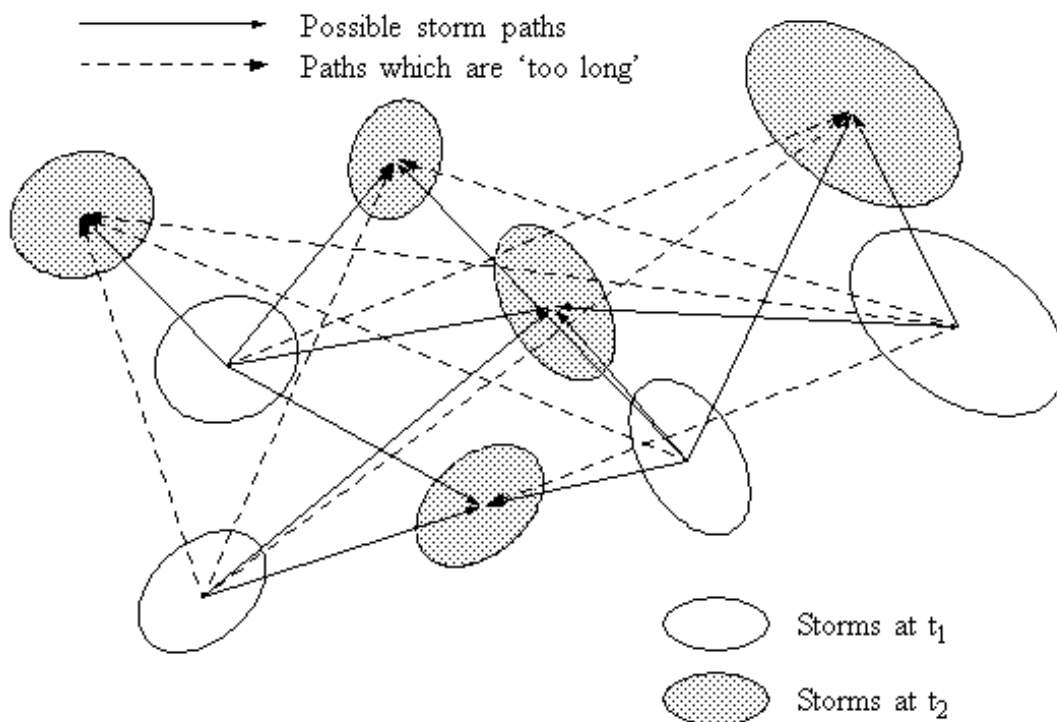


Figure 8. Scheme of TITAN (Dixon et al., 1993).

Some works were made in order to estimate the evolution of the intensity and area, but they didn't converge to a real improvement of the results. They concluded that essential physical processes that dictate the change in rainfall with time are not necessarily observable in the past history of a particular echo development (Tsonis et al., 1981).

Cell centroid methods use an extrapolation of the centroid path in order to do the forecast.

### **2.3.3. Operational Nowcasting Techniques**

The anterior techniques have been further developed and applied to radar data. For cell centroid technique, newer versions of TITAN (Dixon et al., 1993) had been developed. In this versions, the shape of the storm modelled by ellipses had been substituted by a polygon. Moreover, TITAN provides a way to handle mergers and splits (see section 3.2.2.3). Storm forecasts are made by extrapolation of the storm position and other storm properties, as for example volume. Nowadays, TITAN is one of the most used algorithms in meteorological services (Reyniers, 2008).

Another operational cell tracking technique is SCIT (Storm Cell Identification and Tracking; Johnson et al., 1998). It works with several reflectivity thresholds for the cell detection and only uses a distance criterion to match storms at different times based on the storm position predicted with a velocity estimated from anterior scans. This technique performs well for convective cells, but fails in mesoscale stratiform precipitation areas.

A third interesting cell technique is TRT (Thunderstorm Radar Tracking algorithm; Hering et al., 2004; 2005; 2006), which uses an adaptive thresholding scheme (Reyniers, 2008). This allows to detect the storm stages of development.

By the other side, for area tracking techniques COTREC/TREC has been extensively optimized (Mecklenburg et al., 2002) and VET (Variational Echo Tracking) has been developed and improved as part of the McGill Algorithm for Precipitation Nowcasting Using Semi-Lagrangian Extrapolation (MAPLE) (Germann et al., 2002).

There also were developed nowcasting techniques applied to satellite data (like MASCOTTE (Carvalho et al., 2001) or Cb-TRAM algorithm (Cumulonim Bus Tracking And Monitoring) (Zinner et al., 2008) where the tracking is based on geographical overlap between current detections and first guess patterns of cells predicted from preceding time steps.

Furthermore, there are also algorithms that use lightning data as basis for the storm detection and tracking, for example the algorithm developed by Steinacker et al., 2000.

There was an intent to compare different operational nowcasting systems in Sydney 2000, known as Sydney 2000 Forecast Demonstration Project. There were tested some operational and under development nowcasting systems, as for example TITAN (Dixon et al., 1993), NIMROD (Golding, 1998), GANDOLF (Pierce et al., 2000), ANC (Mueller et al., 2003) and S-PROG (Seed, 2003). The general conclusion of this experiment was (from Pierce et al., 2004): “. . . , *nowcasting algorithms based upon the linear extrapolation of observed precipitation motion (Lagrangian persistence) were generally superior to more sophisticated, nonlinear nowcasting methods. Centroid trackers (TITAN) and pattern matching extrapolators using multiple vectors (Auto-nowcaster and Nimrod) were most reliable in convective scenarios. During widespread, stratiform rain events, the pattern matching extrapolators were superior to centroid trackers and wind advection techniques (Gandolf, Nimrod).*”

### 3. METHODOLOGY

In the following, the methodology that has been developed will be explained in detail. This includes the description of the data used and the five main blocks of development in which the development of the system has been structured. These main blocks are:

- 1) Storm detection. In this part, convective cells are defined in the radar image.
- 2) Storm tracking and history derivation, in which thunderstorms are identified and followed from radar observations at different times.
- 3) Short-term forecasts. Here the extrapolation of the cells at future times is performed from last radar observation.
- 4) Alarm generation for the airport area. In this block, it is developed an algorithm that automatically generates alarms when a forecasted thunderstorm hits the airport.
- 5) System evaluation. Finally, a statistical evaluation of the system performance is carried out, using some commonly used skill scores (specified in section 3.2.5).

#### 3.1. Data

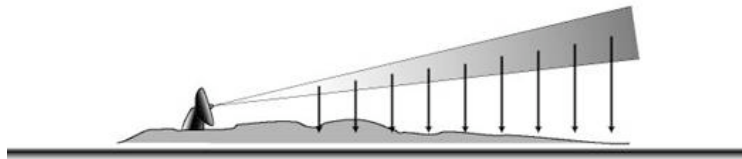
The alarm system developed within this thesis is based on radar observations of the radar composite of Catalonia. A radar composite is available in real time every 6 minutes from the 4 radars from the XRAD (Xarxa de Radars del Servei Meteorològic de Catalunya). The XRAD is made up of the radars of Vallirana, Puig d'Arques, La Panadella and Tivissa-Llaberia. The location of the radars is represented in Figure 9.



Figure 9. Location of the radars of the XRAD (Source: Servei Meteorològic de Catalunya)

Data from each individual radar have been corrected for ground clutter (Berenguer et al., 2006), mountain screening effects (Delrieu et al., 1995), and speckles and signal stability (Sempere-Torres et al., 2003).

The radar product used here is the composition of the extrapolation to the ground of the lowest PPI of the radars (as shown in Figure 10). Different schemes of extrapolation are used depending on the type of precipitation. For stratiform regions, the mean value of the VPRs (Vertical Profiles of Reflectivity) measured near the radar is used as pattern for the farthest regions. For convective regions, the reflectivity at the ground is the radar lowest reflectivity measure (direct extrapolation) (Franco et al., 2006).



**Figure 10. Scheme of extrapolation to the ground of the lowest PPI (Source: Sánchez-Diezma, 2001)**

The composition of the data of the individual radars is made by maximum. It means that for every pixel on the image the maximum reflectivity value of the four radars is taken.

An example of reflectivity field radar product is provided at Figure 11.

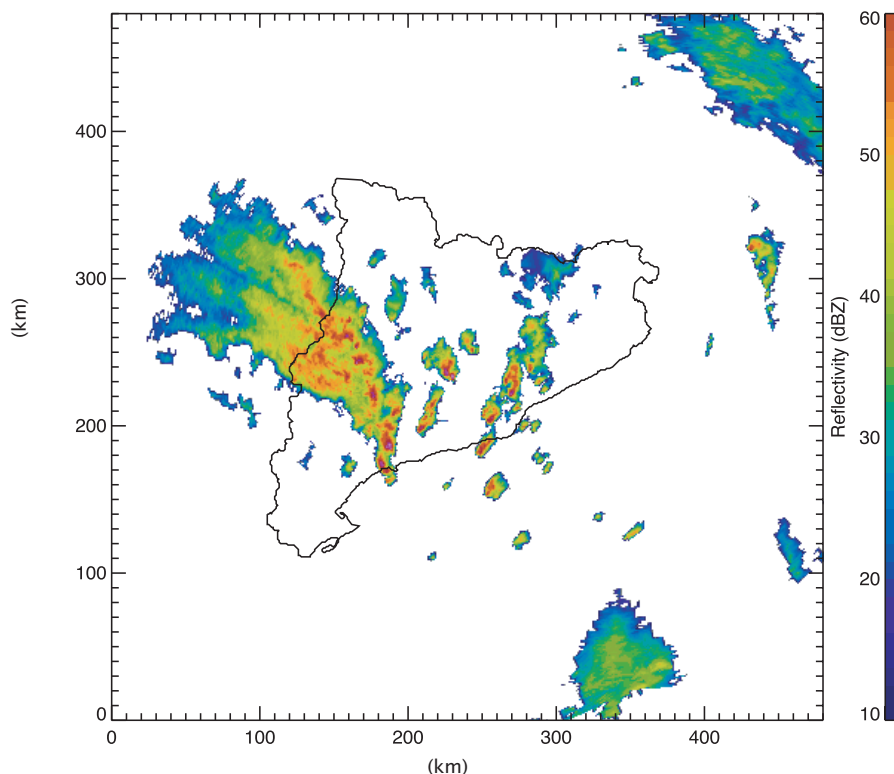


**Figure 11. Reflectivity field for the 10 October 2005 at 10:00 UTC, obtained from the composition of the four radar of the XRAD network.**

## 3.2. Main Blocks of the Alarm System Development

### 3.2.1. Storm Detection

The starting point of the system is to detect and identify storms. As known, in the radar reflectivity fields used, the information is given as the intensity of the reflection as function of the position. A way to detect convective cells is by means of applying a reflectivity threshold. So all the image pixels that exceed it are defined as possible storms. Then all adjacent pixels are defined as the same thunderstorm and it is obtained the cell contour. Thus, storms are defined as polygons.

Depending on the threshold used, the features of the thunderstorms detected are going to change, and usually the higher the reflectivity threshold applied, the shorter the thunderstorm time of life. The threshold used here is 35 dBZ because it allows the detection of convective phenomena and, at the same time, ensures a proper cell size and lifetime to be tracked.

Furthermore, a criterion of storm minimum area is also applied in order to make sure that we really detect thunderstorm cells, and not other objects like airplanes or birds. In our case, areas lower than 50 km<sup>2</sup> are not considered to be storms in our system.

An example of storm detection is provided in Figure 12. It can be observed that regions that exceed 35 dBZ (contours represented in magenta) are modelled as storm regions.

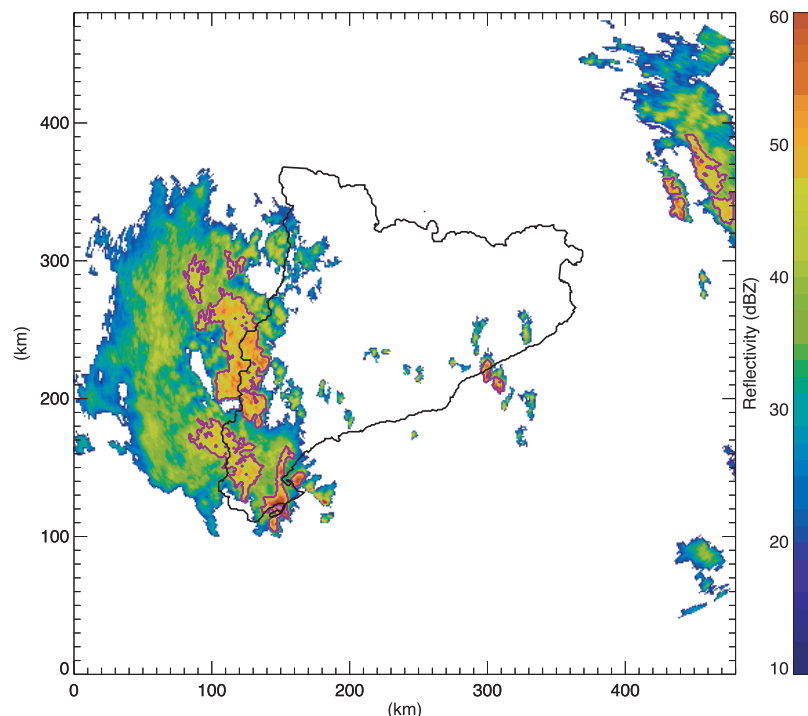


Figure 12. Example of cell detection. Reflectivity image from 15 October 2005 at 12:00h UTC superposed by the storms contours (magenta).

## 3.2.2. Storm Tracking and History Derivation

### 3.2.2.1 Storm Tracking

Once the cells have been detected, the next step is to match storms regions detected in consecutive observations in time, in order to obtain the history of the features of each storm for all its life time until the time of last observation.

The basic tracking principle is the determination of the maximum overlap between the cells observed at a certain step of time and the extrapolation of the cells observed at an earlier step of time.

So the tracking of the cells is based on two past radar observations (at time  $t$  and  $t+1$ ), from which a displacement vector field is derived. Applying it to the first observation (at time  $t$ ) it is possible to obtain an expected pattern of the storms at time  $t+1$  (first guess  $t+1$ ). This process is shown in Figure 13.

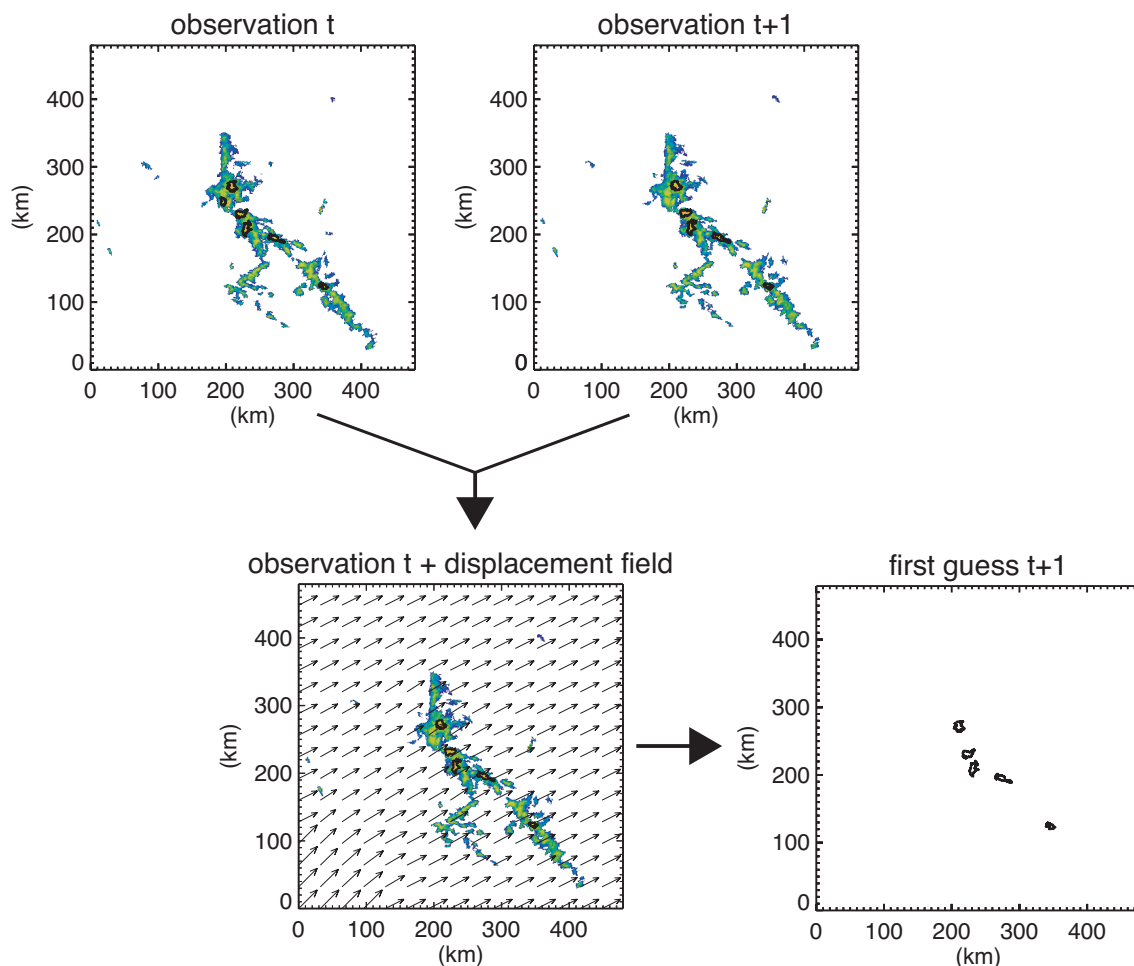


**Figure 13.** Scheme of the procedure of the first guess  $t+1$  derivation. The images correspond to the 12 October 2005 at 16:00h UTC (observation  $t$ ) and 16:06h UTC (observation  $t+1$ ). The contours of the detected cells are depicted in black. The panel located below at the left corresponds to the reflectivity field of observation  $t$  superposed by the displacement vectors found between the two fields. Last panel shows the contours of the estimated convective cells at time  $t+1$ .

For each pattern detected at time  $t+1$  the maximum overlap with the extrapolated cell patterns detected at time  $t$  is determined, and cells with maximum overlap between them are matched.

The three parts of the matching process are detailed as follows:

a) Derivation of the displacement vector field.

The displacement vector field is derived with an algorithm (Berenguer, 2008) that finds the motion field between two reflectivity fields by means of pattern recognition technique using cross-correlation analysis. It is based on Tracking Radar Echoes by Correlation (TREC; Rinehart et al., 1978).

The algorithm works in different levels, each of them defines the number of parts ( $n$ ) in which the image is divided. For a level  $i$ , the number of divisions of the image (windows) is:

$$n = (2^{i+1} - 1)^2$$

And the size of each part is:

$$Lx_i = Ly_i = \frac{L}{2^i}$$

where  $L$  is the size of the original image.

For each level, the displacement vector field is computed with a certain resolution. Starting for the entire image (level 0) it is possible to obtain the desired resolution, because each routine level is initialized with the displacement vector derived on the anterior level. It is important to define the number of levels considering the best agreement between error and resolution. The more resolution, the easier is to find false correlation between windows.

In this work the maximum level used is  $i = 3$ , that means 225 windows ( $15 \times 15$  arrays) of 30 pixels of length.

Finally, COTREC is applied to assure the continuity between vectors.

In order to have the displacement vector field of the same dimensions than the reflectivity image ( $480 \times 480 \text{ km}^2$ ), it is linearly interpolated. The final motion field resulting is a vectorial field of dimensions  $480 \times 480 \text{ km}^2$ .

An example of displacement field is provided in the third panel of Figure 13.

b) First guess pattern derivation

The first guess storm pattern is obtained by means of extrapolating the cells identified at observation  $t$  with the movement of the cell centroid computed using the velocity field obtained from the two last observations (as seen in third panel of Figure 13). Last panel of Figure 13 provide an example of first guess pattern generation.

c) Maximum overlap determination

Once the first guess pattern of the cells at  $t+1$  is derived, the next step is to search the overlap between cells at observation  $t+1$  and first guess  $t+1$ .

In order to do it, the coefficient of overlap is defined:

$$overlap = \frac{area\_overlap}{area\_observation + area\_fg - area\_overlap}$$

where the *area\_overlap* is the area of overlap between a cell at first guess  $t+1$  and a cell of observation at  $t+1$ . *Area\_observation* and *area\_fg* are the area of the cell observed at  $t+1$  and the area of cell pattern at first guess  $t+1$ , respectively.

**Figure 14** represents the tracking principle. In the figure, the cell observed at time  $t$  and time  $t+1$  are represented in black, and the first guess of the cell at  $t+1$  derived from observation at  $t$  is represented in gray. The overlap between first guess  $t+1$  and observation at  $t+1$  is the plotted area.

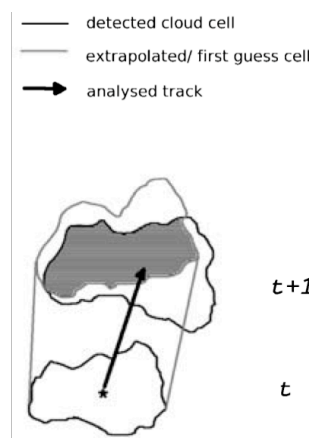


**Figure 14. Scheme of the tracking principle: observations at time  $t$  and  $t+1$  are represented in black, and first guess extrapolation at time  $t+1$  in gray. The plotted area represents the overlap. (Zinner et al., 2008)**

For every observed cell at time  $t+1$ , the overlap with all cells from first guess is computed. If no overlap is found, the cell is assumed to be a new one. If more than one cell overlaps, only the one with the maximum overlap is assumed to be the same one.

A condition of minimum overlap is applied to match two storms. If the overlap coefficient is minor than a minimum overlap, the cell is also assumed to be a new one.

### 3.2.2.2. Storm Attributes and History Derivation

With the anterior procedure, storms at different observation times are identified. Each storm is then named with a tracking identification number, which is the object number and should be unique. The format used in this thesis is YYYYMMDD.HHMM.NNNN. It means:

YYYYMMDD: the date of the first detection of this cell

HHMM: the time of the first detection of this cell

NNNN: cell number/identifier (obtained from the detection algorithm)

For each convective cell, its history is derived. The history consists in a group of features (computed for each thunderstorm and each observation) that characterize the thunderstorm, and have importance for aviation and airport management.

The attributes computed in this study are:

- Area covered
- Centroid position
- Moving direction of the cell centroid
- Moving speed of the cell centroid
- Maximum reflectivity
- Cell contour positions

The result is a list of features for every thunderstorm. In next figure, an example of cell tracking is represented. Each colour represents the contour of a thunderstorm detected at the observation time, while the black lines represents the track of each cell (the history of the cell centroid).

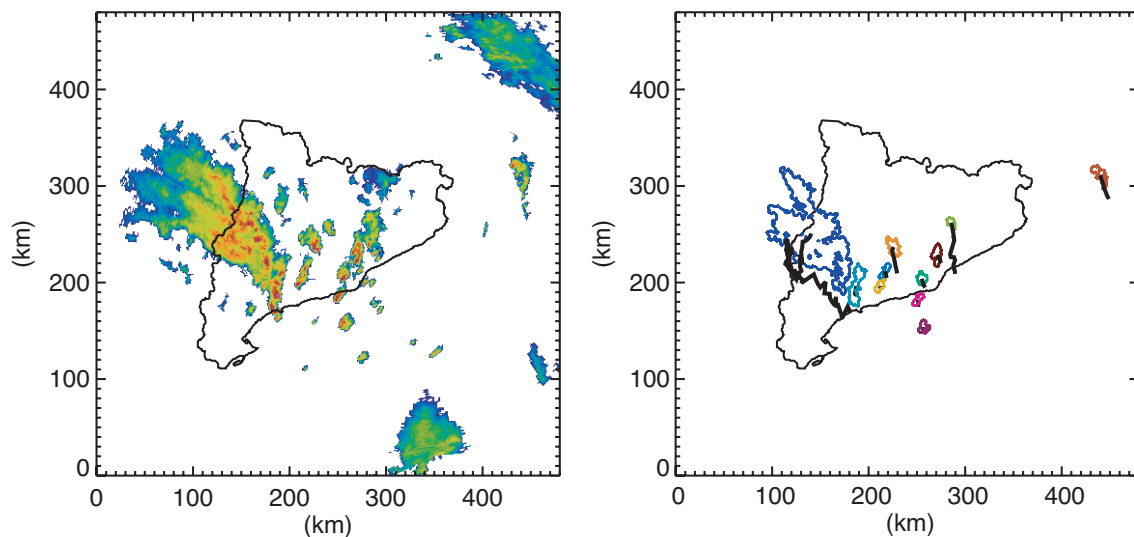


**Figure 15. Cell tracking example. Left panel represents the reflectivity field of the 15 October 2005 at 12:00h UTC. Panel on the right represents all the cells detected on this observation and the cell track (history of the cell centroid) for each one. Longer cell tracks represent longer life times. Different colours represent different cells.**

With these computed properties it is possible to obtain the qualitative statement on the development of the horizontal extent of the object (“decaying”, “constant”, or “growing”) and the history of the cell centroid, a row of values that contains the track history of the storm.

This information will be used to characterize the storms. It is saved in a xml file for each radar image observation. Each file contains a list with the existing storms and its particular history (the list of attributes named before).

### 3.2.2.3. Mergers and Splits

When tracking storms, sometimes it is found that more than one storm merge to a single thunderstorm cell. The same way, but less frequently, it happens that a unique storm split up in two or more separated thunderstorm cells.

In order to track these kinds of cells, a criterion to handle them is needed. The one used here is (Dixon et al., 1993):

For mergers, only the history of the thunderstorm cell with maximum overlap is going to be continued, while the history of the other ones is going to be terminated (see Figure 16a).

For splits, only the storm with biggest overlap is going to inherit the history, while the others are going to be treated as new ones (see Figure 16b).

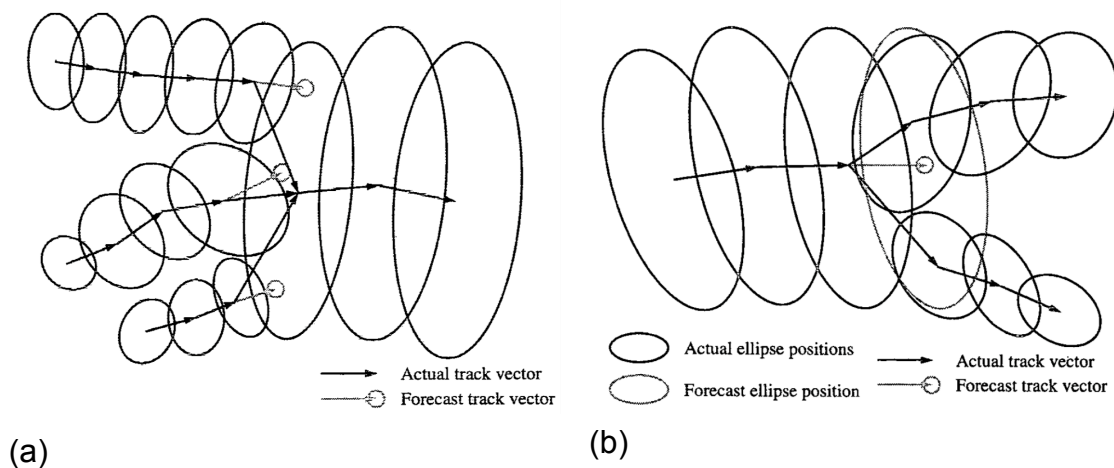


**Figure 16. (a) Merging of three storms to a unique cell (b) Split of a convective cell into two different cells. In these images, convective cells are modelled as ellipses (source: TITAN, Dixon et al., 1993)**

### 3.2.3. Nowcasting

The forecast is implemented by means of extrapolating the last reflectivity field observed. The algorithm that performs it (Berenguer et al., 2008), advects the last observed reflectivity field using the computed motion field between the last two observations with the algorithm explained at section 3.2.2.1. The scheme of the forecast is shown in Figure 17. The figure shows how from the last two observations (second and third panels of first row) the motion field is obtained, and how applying it to the last observation (second row panel) a forecast at different times is generated (third row panels).

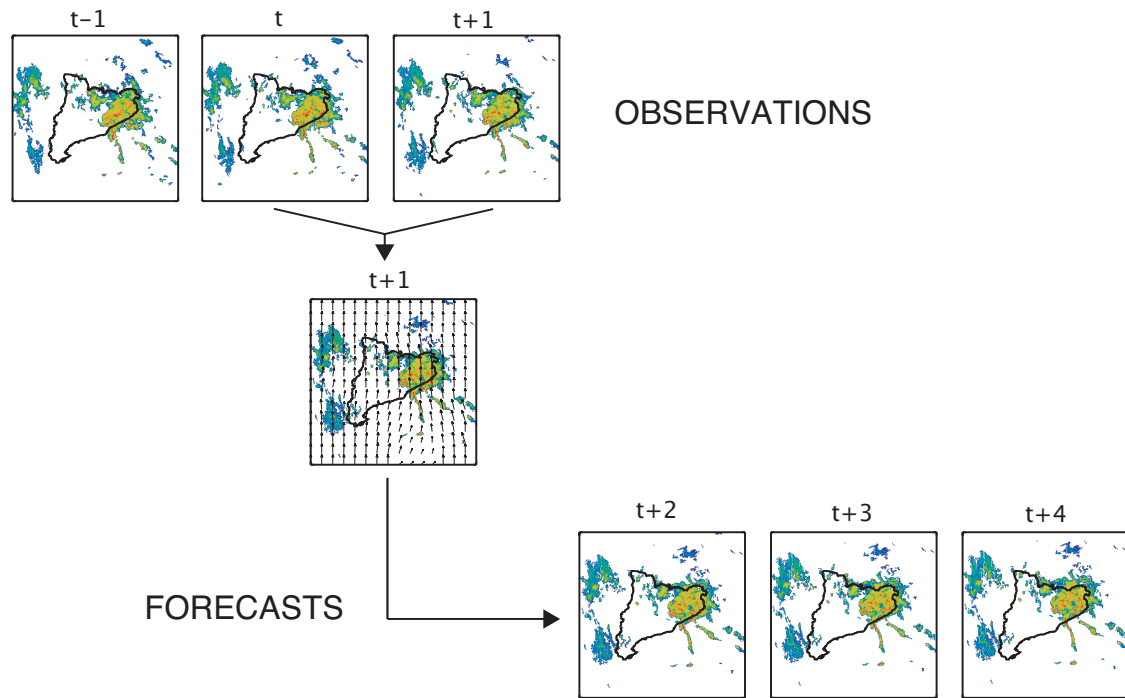


**Figure 17. Scheme of the procedure to extrapolate the observations. In the first row there are represented the observations until time  $t+1$ . The second row shows the reflectivity field observed at time  $t+1$ , plus the velocity field generated from observations  $t$  and  $t+1$ . Forecasts for times  $t+2$ ,  $t+3$  and  $t+4$  are represented in the last row.**

There exist two ways of doing the forecast: forward and backward. In a forward scheme, we move the pixel that occupies the grid point on the origin of the displacement vector to the grid point on its ending. In a backward scheme, we determine the origin of a parcel that would end up at the grid point where the displacement vector ends. This kind of extrapolation makes sure that every pixel of the forecasted images will always have only one intensity value associated, whereas in the forward extrapolation a forecasted pixel could have more than one intensity value associated, or could not have any.

The drawback of the method is that the area of the forecasted fields is reduced more and more as larger is the lead time (Figure 18).

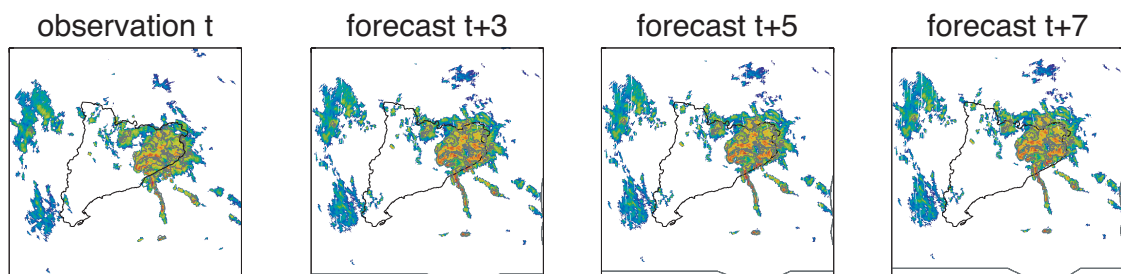


**Figure 18. The figure shows the observation of 13 October 2005 at 2:24h UTC (first panel) from which the forecasts are derived (last three panels). It is possible to observe how the area is reduced in forecasts generated with a backward scheme (areas below the gray line at the panel bottoms don't provide any information about the reflectivity field).**

The extrapolation is performed pixel by pixel with semi-Lagrangian persistence. That means that the displacement vectors used to extrapolate the reflectivity field will be considered stationary during the forecast time, so they are going to be the same vectors for all the forecasts initialized at the same time.

While rotations are not considered using a constant-vector scheme ( $\vec{\alpha} = \tau \vec{u}(t_0, \vec{x})$ , where  $\vec{\alpha}$  is the displacement vector,  $\tau$  the lead time and  $\vec{u}$  is the echo motion at point  $\vec{x}$ ) semi-Lagrangian scheme allows movements of rotation. In this model the advection is divided into  $N$  steps of length  $\Delta t$  where  $N\Delta t = \tau$ . The displacement vector is computed in  $N$  iterations as follows:

$$\vec{\alpha} = \Delta t \vec{u} \left( t_0, \vec{x} - \frac{\vec{\alpha}}{2} \right)$$

Starting with  $\vec{\alpha} = 0$  (the displacement vector in the first iteration is the corresponding to the pixel  $\vec{x}$ ), the displacement vector in each iteration is used in the next one to compute the pixel for which the displacement vector is going to be computed. Then, the final displacement vector is the vectorial sum of all the computed vectors. So, depending on the lead time we are going more or less further in time using only one velocity field.

An example of the displacement vectors of four advection schemes (combinations of the schemes mentioned in this section) are presented in Figure 19 (Germann et al., 2002).

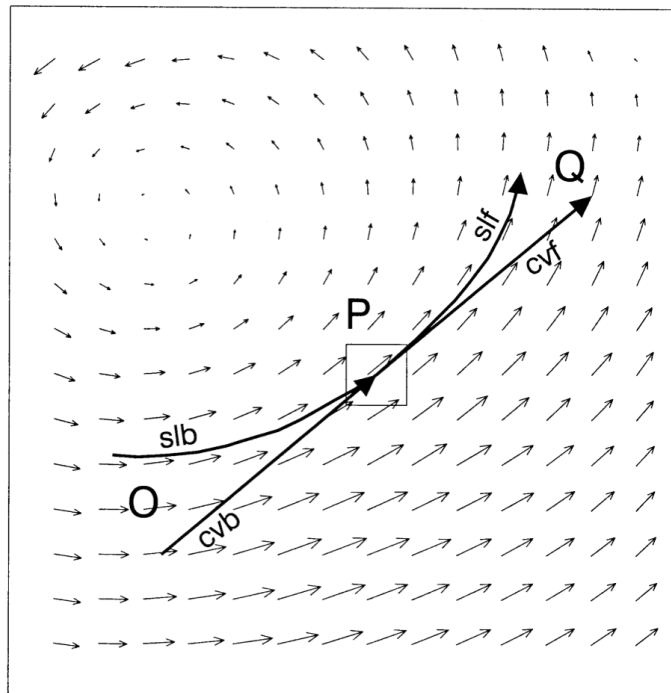


Figure 19. Displacements vectors of four advection schemes: slb (semi-Lagrangian backwards), slf (semi-Lagrangian forward), cvb (constant vector backwards), and cvf (constant vector forward) (Source: Germann et al., 2002)

Figure 19 illustrates the fact that semi-Lagrangian scheme allows rotation movements while constant vector scheme does not. Moreover, it provides a clear example of backward and forward extrapolation operation, where the pixel advected is the one at position 0 in backwards extrapolation, and the one at position P in forward scheme.

Because of the reasons mentioned before, the scheme of our extrapolation is a semi-Lagrangian backward scheme. The advected field will be  $\bar{\Psi}(t_0 + \tau, \vec{x}) = \Psi(t_0, \vec{x} - \vec{\alpha})$  (Germann et al., 2002).

In the scheme of extrapolation that we are going to use, total intensity remains unchanged, so storm intensity changes are not considered.

In this work, we want a forecast every 6 minutes, from the time of the last observation until 60 minutes after it. The resolution time of the algorithm is equal to 1 minute. The shorter the resolution, the more precise the result, but also the larger the time used to carry out the computations.

### 3.2.4. Alarm Generation

The final step for the development of the system is the generation of an algorithm that defines alarms for the airport. Alarms are automatically generated when forecasted thunderstorms hit the airport area. So, after each observation, the system makes forecasts from 6 to 48 minutes (for every 6 minutes) and, for each of these lead times, the system checks if any thunderstorm hits the airport.

The airport area is defined as the area of the airport itself (16 km<sup>2</sup>) plus a security area (1 km surrounding the airport). In total, the airport area defined in this master thesis is 36 km<sup>2</sup> (6 km x 6 km).

As said before, the system will provide information about all the thunderstorms near the airport individually and its features, so alarms should give the information necessary for the airport controllers and management, such as the storm velocity, its maximum intensity, the trend on area and the forecasted time of the storm hitting the airport.

### 3.2.5. Evaluation of the System

The evaluation of the method is performed on the basis of the commonly used statistical skill scores POD (Probability of Detection), CSI (Critical Success Index) and FAR (False Alarm Ratio). They are applied to dichotomous (yes/no) forecasts (in this work if the storm enters or not the airport area).

In order to define the skill scores we need to define the possible combinations of forecasts (yes or no) and observations (yes or no). There are four combinations, which are represented in Table 1.

Forecasted	Observed	
	Yes	No
Yes	hit	False alarm
No	miss	Correct negative

**Table 1. Hit, false alarm, miss and correct negative forecasts definitions.**

They are defined as follows:

Hit: event forecasted to occur, and did occur

Miss: event forecasted not to occur, but did occur

False alarm: event forecasted to occur, but did not occur

Correct negative: event forecasted not to occur, and did not occur

Using the table, it is possible to proceed to some statistical studies depending on the aspect of interest of the forecasts. Their range goes from 0 to 1. The indexes used in this work are:

POD is the probability of detection. It is a measure of the hit rate, in other words, the fraction of the observations that were forecasted properly.

$$POD = \frac{Hits}{Hits + Misses}$$

The perfect score would be 1, and it would mean that all the events that were positive in the observations were correctly forecasted.

FAR is the False Alarm Ratio, and it is an indicator of the rate of positive forecasts that actually didn't happen.

$$FAR = \frac{FalseAlarms}{Hits + FalseAlarms}$$

The perfect score is 0.

FAR and POD should be used in combination because they provide complementary information.

CSI is the Critical Success Index. It measures the fraction of observed and/or forecasted events that were correctly predicted. Sensitive to hits, penalizes both misses and false alarms.

$$CSI = \frac{Hits}{Hits + FalseAlarms + Misses}$$

The perfect score is 1.

In order to have a statistical verification of the system (due to the fact that it is difficult to find a number of study cases at the real airport position that allows statistical verification), the previous validation is applied to 100 hypothetical airport areas separated 30 km between them. Each airport has the same dimensions than our original airport. Figure 20 illustrates the hypothetical airports used for the verification.

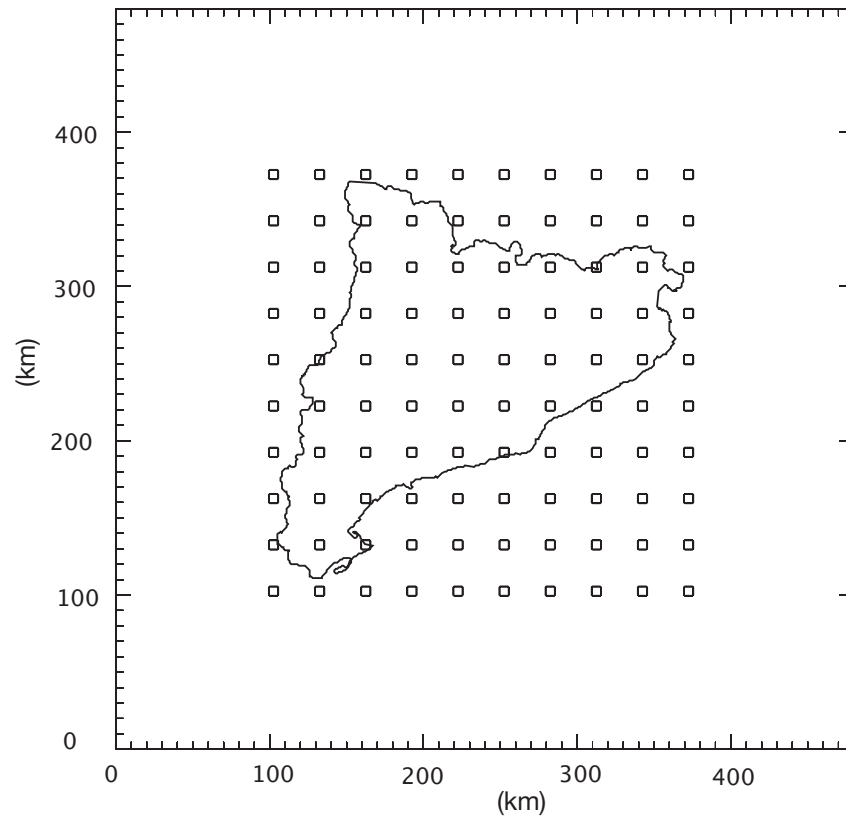


**Figure 20. Location of the 100 hypothetical airport areas for doing the verification.**

It has to be commented that, due to the proximity between verification areas, sometimes it is possible to find some kind of correlation between results. This is because a storm could pass from more than one validation area, so the skill scores would be, in some way, the same for more than one area and it would count more than once to the statistics. However, we consider that in our validation context is totally acceptable.

## 4. RESULTS

The thunderstorm nowcasting alarm system explained in the previous chapters was applied to several study cases. These cases were characterized by presenting some kind of convective activity. For each of these cases, a table with each detected thunderstorm and its attributes was computed. These properties are the first and last time in which they were observed, mean and maximum area, mean velocity, maximum reflectivity reached, and the computed life time. It has to be known that this life time is only an approximated duration, because it is computed from the time of the first and last observation in which it was detected.

In order to illustrate the results obtained, we show here three representative cases, each of them covering one entire day. They are:

- Case 1: 25 June 2009
- Case 2: 15 October 2005
- Case 3: 13 September 2006

### 4.1. Case1: 25 June 2009

During the day 25 June 2009 some convective phenomena took place over Catalonia, mostly during the afternoon hours. Convective phenomena started at night, about 1:00 UTC at the Nord-West of the region (see top left panel of Figure 21). These convective cells dissipated in a few hours, leading to no convective phenomena until noon. Cells began growing and dissipating over the entire region (see top right and bottom left panels of Figure 21) until 19:00 UTC, when convection started to dissipate and finally disappeared about 21:00 UTC (see bottom right panel of Figure 21). In Figure 21 it is possible to observe the general behaviour of the precipitation regions during the day of study.

During this day, 84 regions of intense precipitation (here considered as thunderstorm cells) were detected.

The general characteristic of these cells is that their life time was generally short, as it can be seen in Figure 22a. It has been computed that the 80% of the storms didn't exceed one hour of life and the 46% dissipated in less than 20 minutes. Only 20% of the storms had duration longer than one hour, and only three of them lived more than 2 hours.

In general, regions detected in this case had a generally small horizontal extension. The 94% of the storms had a mean area smaller than 150 km<sup>2</sup> (Figure 22b).

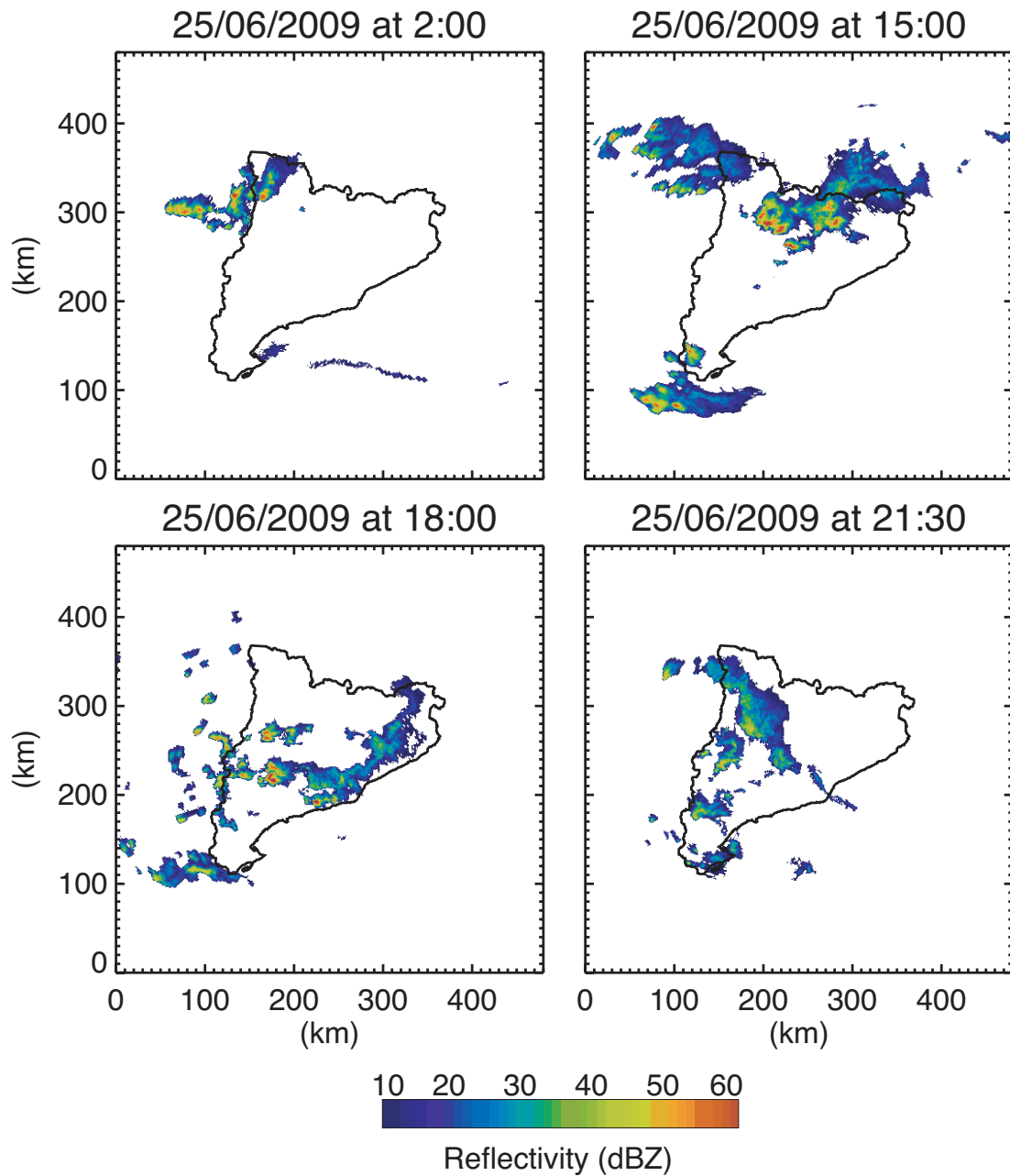
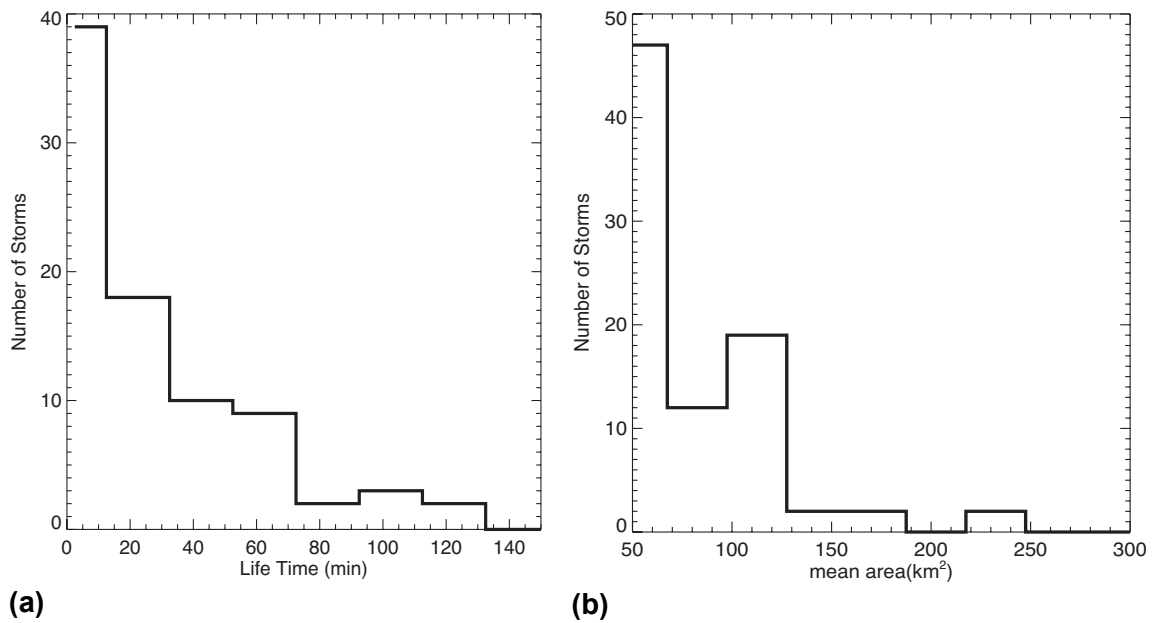


Figure 21. Reflectivity fields observed the 25 June 2009 at 2:00 UTC, 15:00 UTC, 18:00 UTC, and 21:30 UTC.



**Figure 22. (a) Number of storms in function of their life time for the case 25 June 2009 (b) Number of storms in function of their mean area for the case 25 June 2009.**

In Figure 23 it is shown the relation between life time and maximum horizontal extension reached by the storms. It can be seen that most of the storms had short life times and small horizontal extensions. It can also be observed that storms that reached bigger extension had a longer life time.

The correlation computed for the relation between life time and maximum horizontal extension gives a value of 0.83.

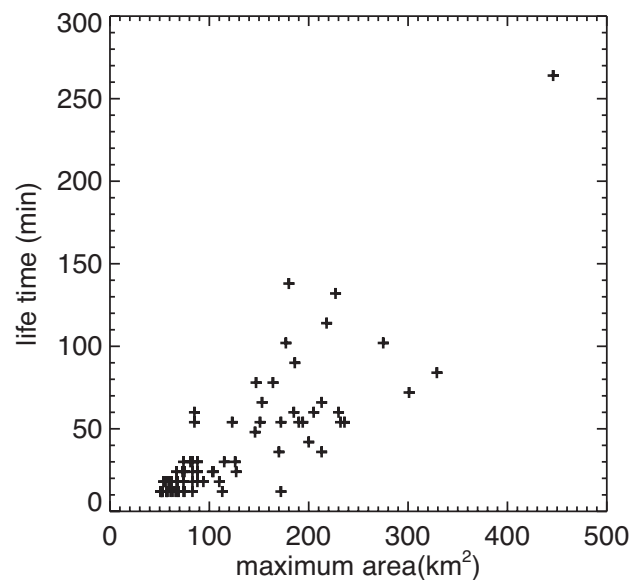


**Figure 23. Storm life times versus maximum extension of the storm for the case 25 June 2009.**

As explained in section 3.2.5, alarms are set just after every radar observation for each forecasted storm that hits an airport. So, the same storm could produce more than one alarm for a same airport. Also, for a certain time it is possible to find more than one alarm due to the same storm forecasted from different reflectivity fields (observations at different times). The reason is that at observation  $t$  the forecast is done for the period from  $t+1$  to  $t+8$ . So, for example, for time  $t+3$  could happen that three alarms were set (from forecast  $t+3$  from observation  $t$ , forecast  $t+2$  from observation  $t+1$ , and forecast  $t+1$  from observation  $t+2$ ). Thus, the total number of alarms set during a day of strong convective activity can be huge.

For example, for this study case the total number of alarms set was 1212. As said before, this is a large number, but it has to be considered that alarms for a same storm and airport are somehow correlated. These alarms were set in 39 different airports. This result shows that convective activity was not uniformly spread over the entire region, but was scattered in different cells not always related between them.

In order to study the behaviour of a single storm and to illustrate how forecast and posterior alarm generation work, the storm with longer life time (approximately 252 minutes) is tracked. This storm was detected for the first time at 13:24h UTC and it was last observed at 17:48h UTC. It reached a maximum area of 227 km<sup>2</sup> and a maximum reflectivity value of 56 dBZ. Its mean velocity was 4 m/s.

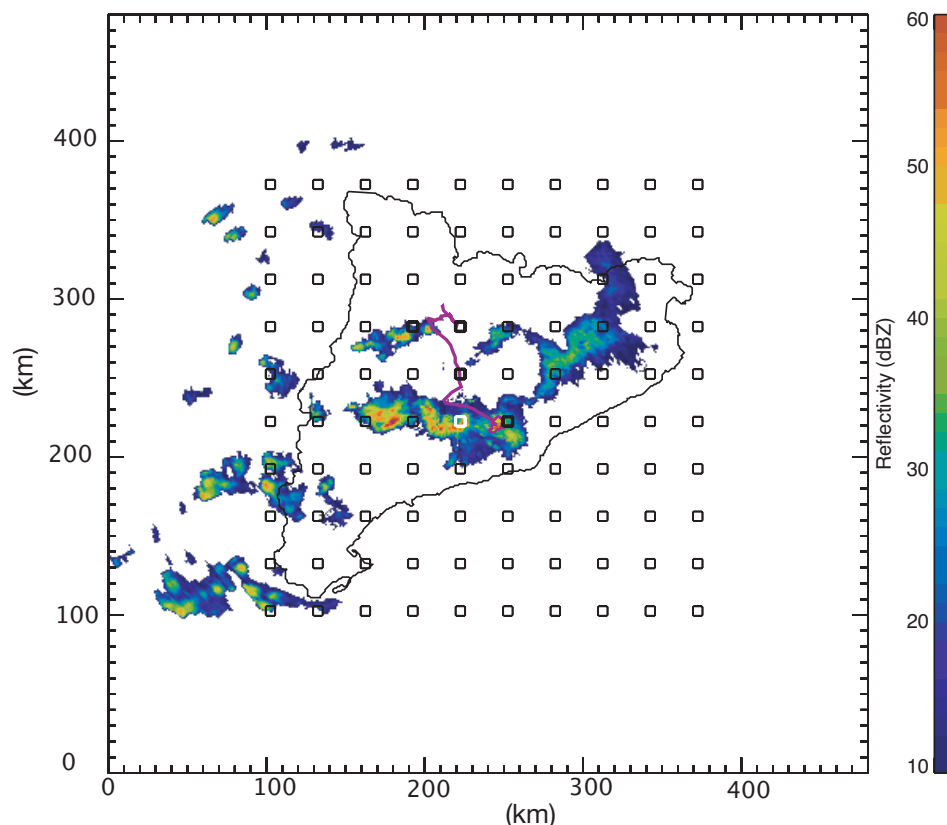


**Figure 24.** Scheme of the track of the studied storm. The image correspond to the reflectivity field at 17:48h UTC of the 25 June 2009. The contour and track of the specific storm is represented in magenta. The contour corresponds to the last detection of the cell and the track shows the storm movement during all its life time.

In Figure 24 is presented the reflectivity field where the storm was last detected (observation at 17:48h UTC). The specific storm contour for the same time is shown in magenta. Its track is also represented in magenta, so it is possible to see the path followed by the cell centroid since it was born.

From the observation of the track in Figure 24, it can be concluded that the movement of the centroid is sometimes erratic (see changes in direction of the track in Figure 24), so difficult to forecast.

This storm hit airports 36, 44, 45, 46 and 54 (as seen in bold and white in Figure 24). Alarms for the storm were set mostly properly in these airports. Moreover, there were false alarms set for another airport in which finally the cell didn't get.

An example of forecast made from observation at 16:06h UTC for the same storm is illustrated in Figure 25. The first panel of the figure shows the observation from which the forecast is set (observation t), and after that, a comparison of the forecasts (second and third panel of first row, and first and second panel of third row of Figure 25) with the observations corresponding to the time of forecast (first and second panel of second row, and first and second panel of fourth row of Figure 25). In black there are represented the cells observed and forecasted, respectively for each field. The contour of the storm that we are studying is plotted in pink.

It can be seen that the main source of errors on the forecasted fields is that growth and decay of the precipitation regions are not considered in the forecast, as explained in section 3.2.3 (see Figure 25). Moreover, changes in intensity are not considered in the forecast, so death of cells is not forecasted (as it can be observed in Figure 25 for forecast t+2), neither its formation (also shown in Figure 25 for forecast t+2, t+4, t+6 and t+8).

By observing the studied storm (pink contour at Figure 25), it can be seen that its shape is constant for all forecasts, while in the observations it keeps growing until time t+4 and after that, it decays.

For this forecast example, it can be seen that the movement of the cell is mostly properly forecasted.

The temporal evolution and performance of the alarms generated for this storm at airport 46 (airport in white at Figure 24), is represented in Figure 26. In the figure, the alarms set for every time step (y axis) are compared to real observations (first row). White colour represents positive cases, that is, when the storm really hit the airport. Each superior row represents the time when forecasts were made and columns represents times for which alarms were set. White rows represents that an alarm was set. So comparing these alarms with the first row, it is possible to see if they were properly forecasted. Alarms set for the same time step of the observations are not represented because they are always a hit. It has to be taken into account that alarms are generated only for lead times from 6 to 48 minutes.

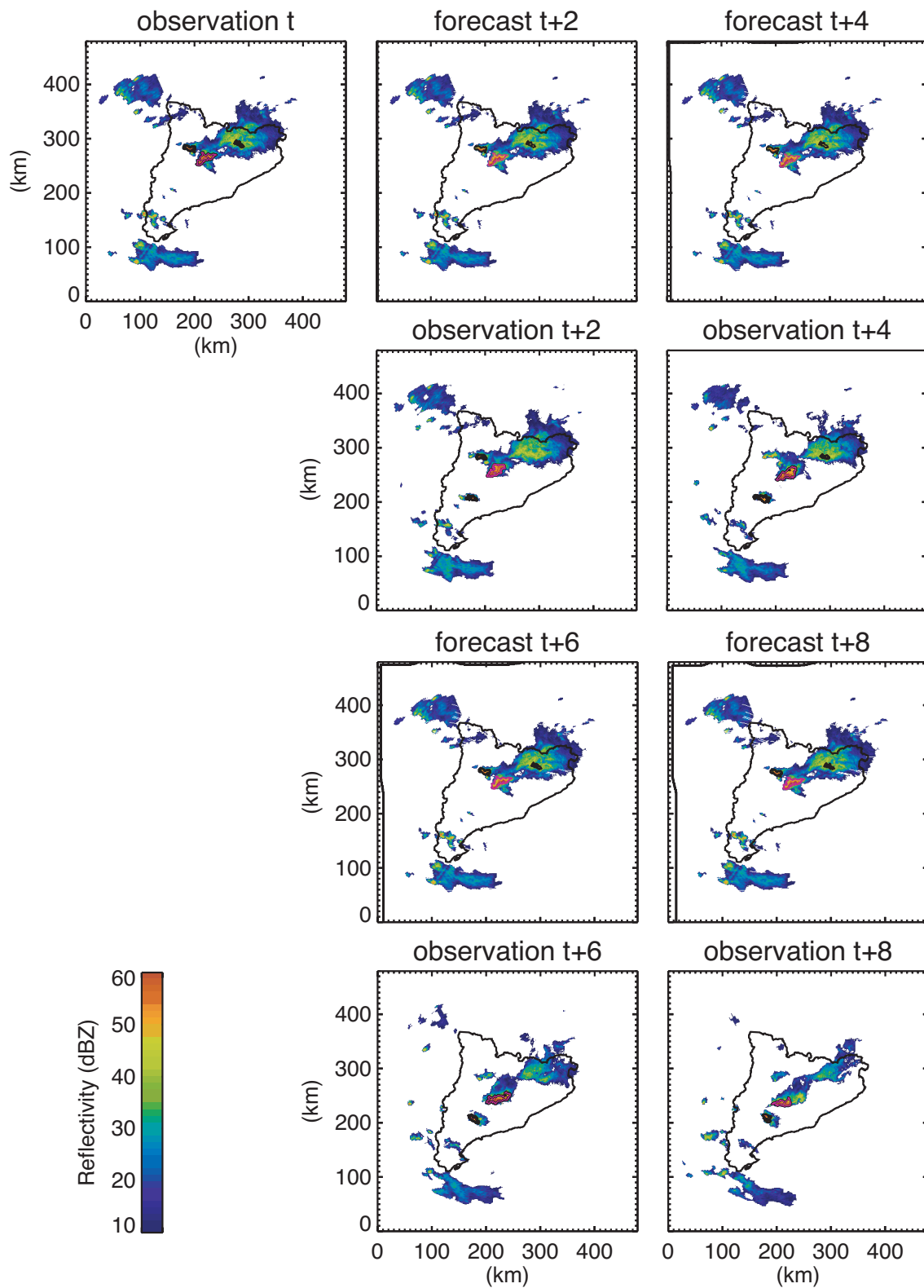


**Figure 25.** Comparison between forecasted and corresponding in time observed reflectivity fields. Forecasts were made from observation of 25 June 2009 at 16:06h UTC, for 16:18h UTC (t+2), 16:30h UTC (t+4), 16:42h UTC (t+6), and 16:54h UTC (t+8). Below every forecasted reflectivity field, the posteriorly observed field is represented.

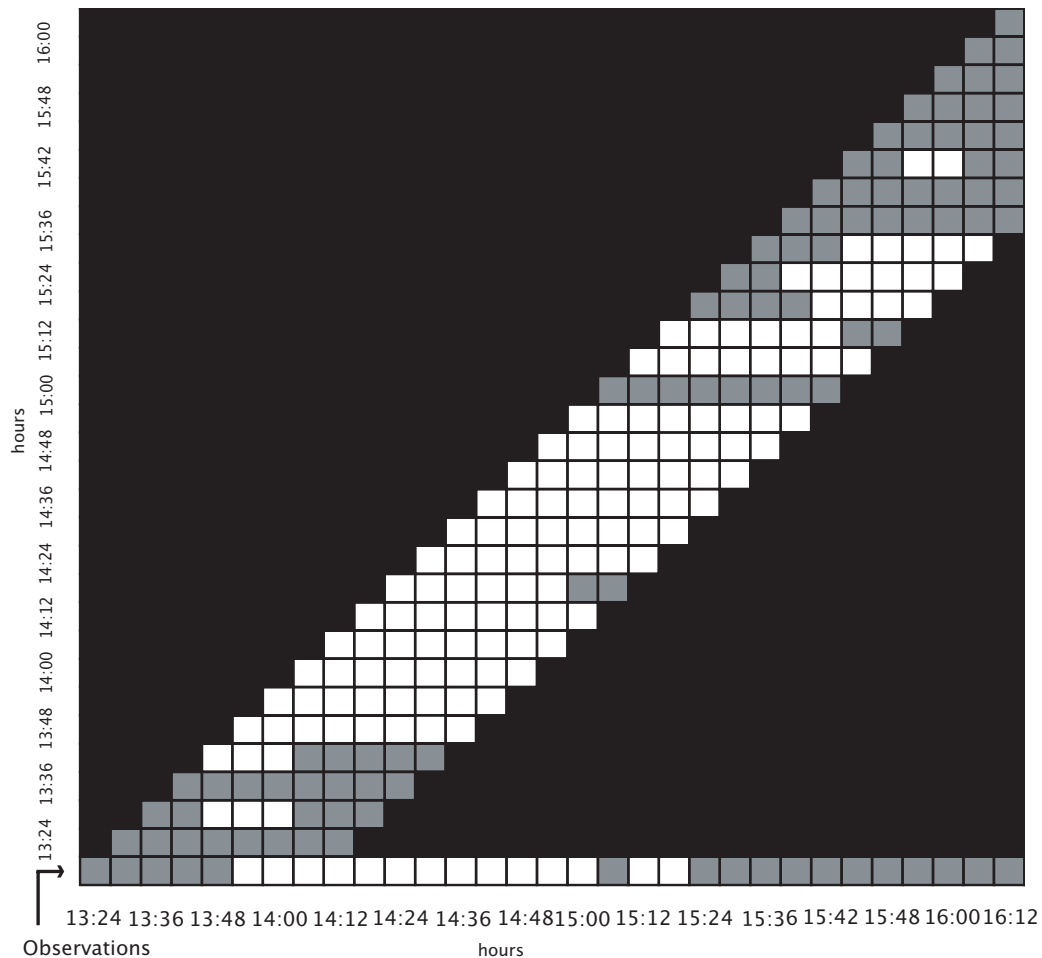


**Figure 26.** Temporal evolution of the alarms set for the specific storm studied at a specific airport (airport 46, in white at Figure 24) the 25 June 2009. The first row represents the observation at the airport. Positive cases (this is, when the thunderstorm did hit the airport) are represented in white, while no alarm set is represented in grey. The other rows represent steps of time for which alarms were generated.

In Figure 26, it is possible to observe the number of hits, misses and false alarms at this airport generated due to the storm. For example, at 13:24h UTC (second row) there were no alarms forecasted, but observing to the observation row, it is seen that the storm hit the airport from 13:54h UTC to 14:12h UTC. So, there were four missed alarms for this time of forecast. But contrarily, at 14:06h (9th row) UTC the system generated alarms for all times of forecast. Comparing to the observation row, it is seen that all of them were correctly forecasted.

In order to have a statistical verification for all the studied day, the mean value of the skill scores POD, FAR and CSI were computed. They have been computed using the total of the hits, false alarms and misses of all the day. The result is shown in Figure 27.

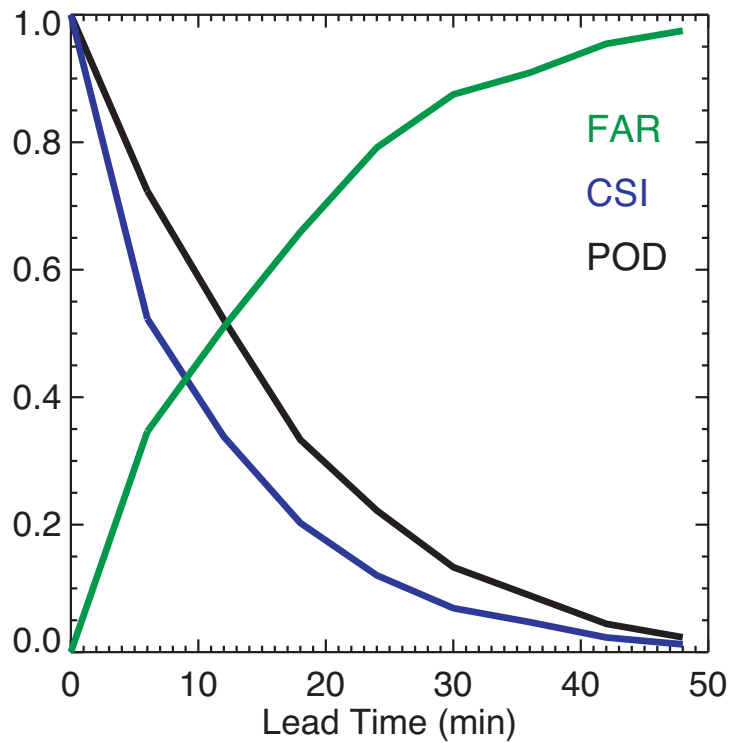


**Figure 27. Mean values of POD (in black), FAR (in green) and CSI (in blue) for the 25 June 2009.**

As the figure shows, the reliability of the system for this case decay rapidly during the first 20 minutes, when POD and CSI indexes decay abruptly and FAR increases very fast. So, in this case, the system gives valuable information until more or less 12 minutes of forecast. This behaviour could be explained due to the short time of life of the storms (as said before, the 46% of the storms lived less than 20 minutes).

## 4.2. Case 2: 15 October 2005

The 15 October 2005 was a day of active convective phenomena that lead to large areas of intense precipitation and strong storms all over Catalonia. During the first hours of the night, some intense precipitation regions formed at the half north of the region (see top left panel of Figure 28) that propagated to the Northeast and finally disappeared. During the morning strong convective cells coming from the Southeast carried on during the following hours propagating and growing to Northwest direction (seen top right and bottom left panels of Figure 28). This general movement changed direction during the afternoon, when the cells began moving to Northeast (see bottom right panel of Figure 28).

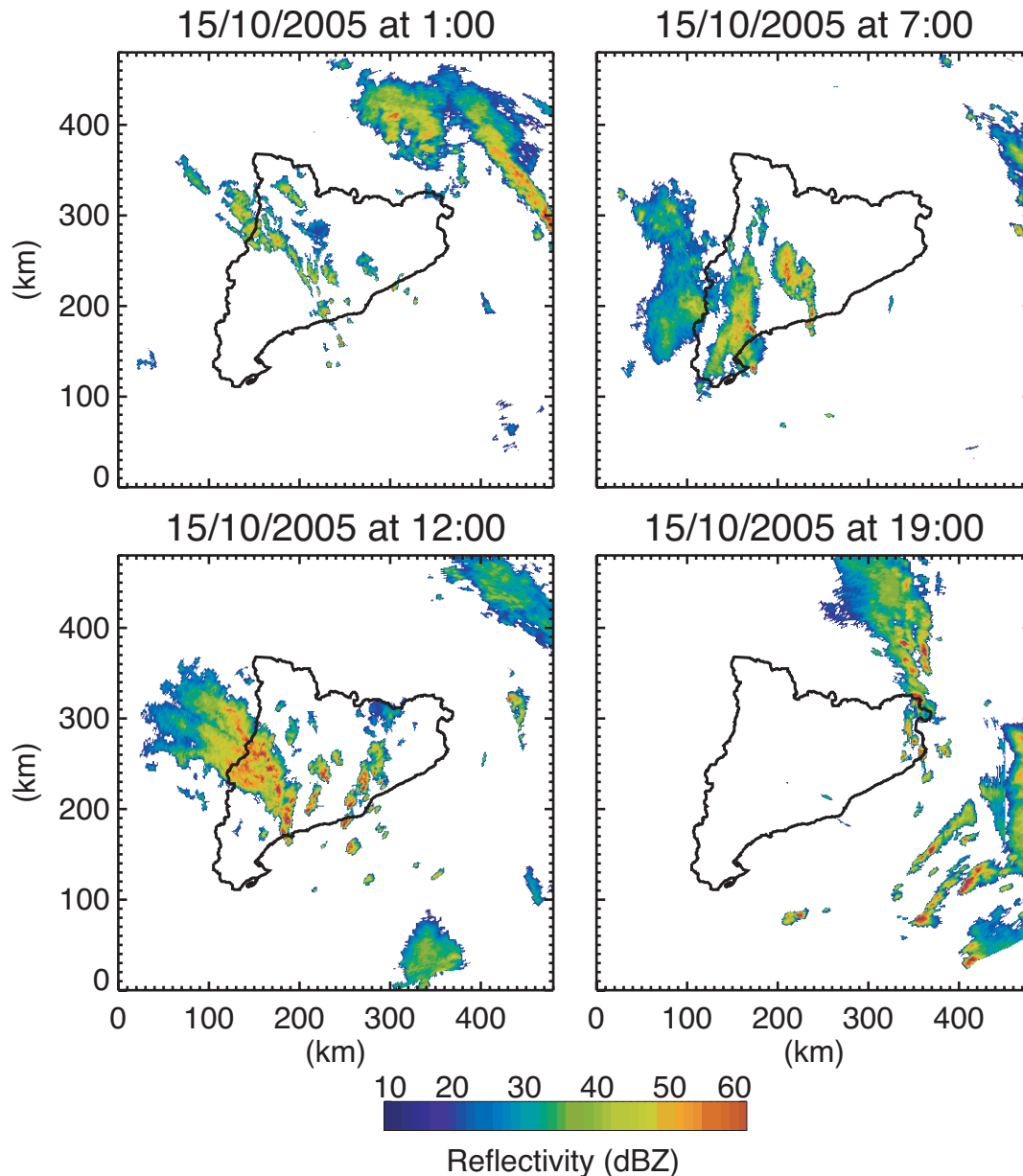
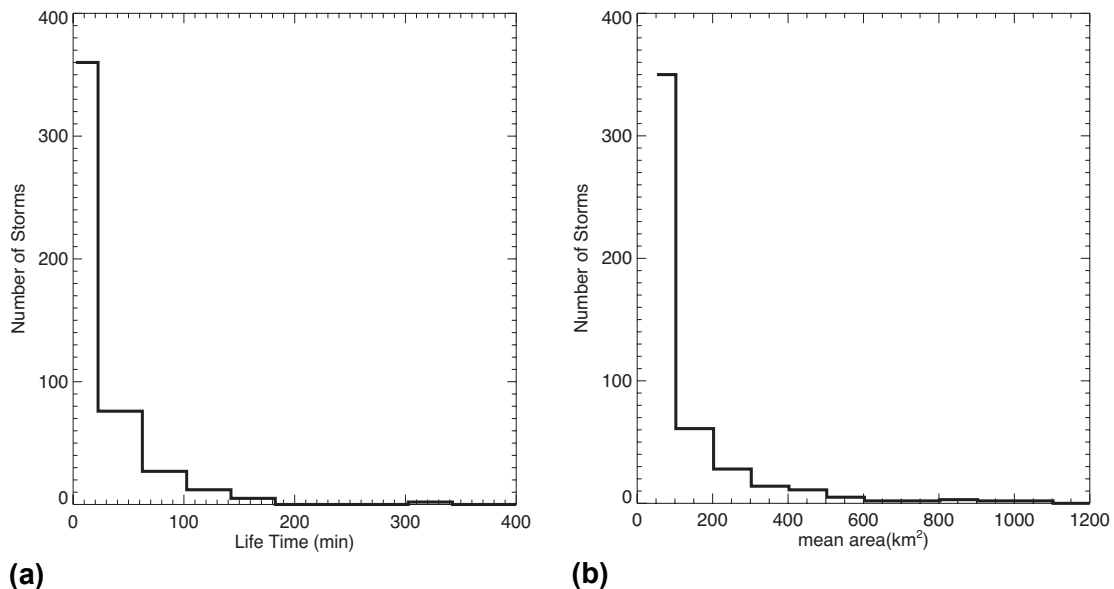


Figure 28. Reflectivity fields observed the 15 October 2005 at 1:00h UTC, 7:00h UTC, 12:00h UTC and 19:00h UTC.

During this case of study, 483 regions of intense precipitation were detected, of which almost 54% lived less than 20 minutes. 83% of the storms lived less than one hour. Only 17 storms lived more than 2 hours (see Figure 29a). The extension of the storms detected were generally large, although 80% of the convective regions detected had mean areas smaller than  $200\text{km}^2$  and 95% smaller than  $500\text{km}^2$  (see Figure 29b).



**Figure 29. (a) Number of storms in function of their life time for the 15 October 2005 (b) Number of storms in function of their mean area for the 15 October 2005.**

In Figure 30 it is represented the life time of the storms in front of the maximum horizontal extension reached. As in the previous case, it can be observed that most of the storms had extensions smaller between 50 and  $500\text{ km}^2$ , and life times inferior to 1 hour. Moreover, as it is expected, storms that reached bigger areas generally had longer life times. Here, the correlation between life time and maximum extension reached is 0.63.

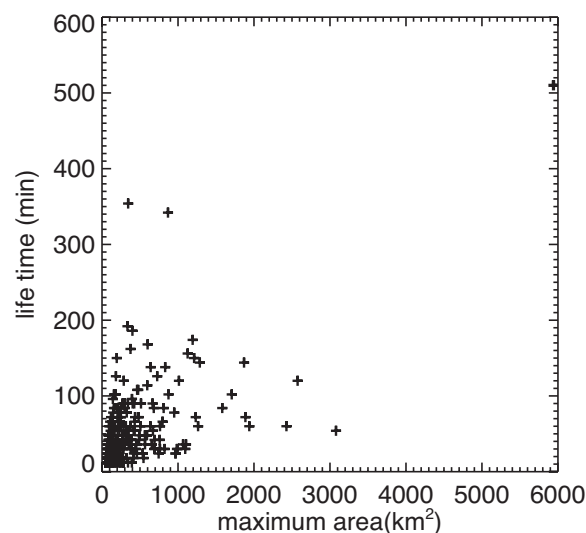


**Figure 30. Storm life times versus maximum horizontal extension for the 15 October 2005.**

For this day, 9586 alarms were set for 83 different airports. As it can be deduced from the number of airports affected by storm alarms, convective phenomena crossed almost all the region covering large areas.

In order to illustrate the nowcasting system performance in a specific case, a specific storm is studied as example. The chosen storm was first detected at 11:12h UTC and its last detection was at 13:30h UTC. The maximum area and reflectivity that it reached were 536 km<sup>2</sup> and 55dBZ respectively, and its mean velocity was 12 m/s.

In Figure 31, the reflectivity field observed at 13:30h UTC (last time when the storm was observed) is represented, with the contour of the storm at this time and its corresponding track represented in magenta. The track shows the history of the cell centroid, because it represents the path that the storm had followed since it was born to its death.

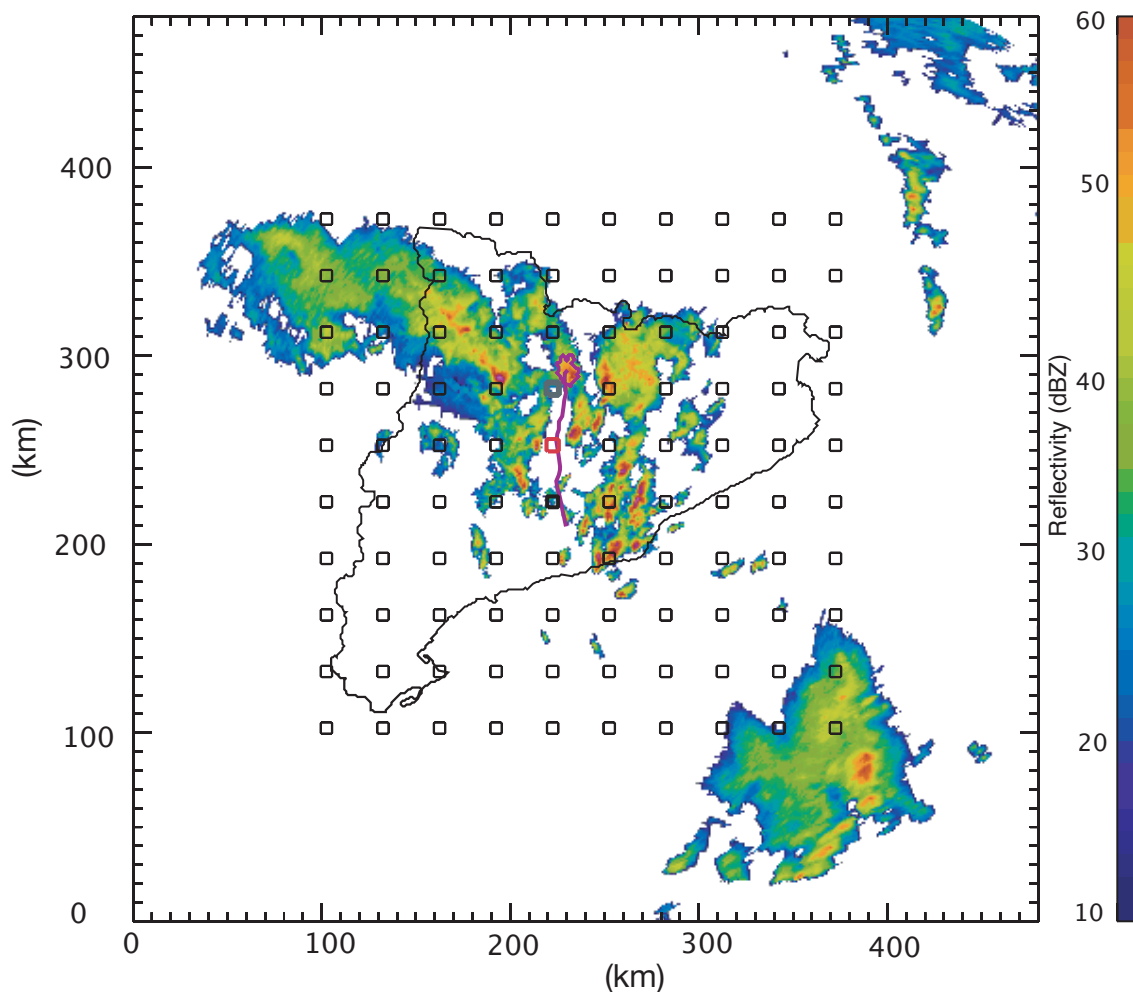


**Figure 31. Reflectivity field of the 15 October 2005 at 13:30h UTC. The studied storm contour at the same time and its track is represented in magenta.**

As it can be seen in the figure, this storm hit airports 44, 45 and 46 (in grey, red and black bold respectively, in Figure 31), and it produced alarms in these airports and also at a last one, in which the thunderstorm didn't get because it dissipated before its arrival.

Figure 32 shows forecasts from 12 minutes up to 48 minutes. As in the previous studied case, it can be observed that the major source of divergence between forecasts and observations is that this model maintains constant the shape of the reflectivity regions. So, the longer the lead time, the more the prediction from the reality diverges. This is easily observable at forecasts t+6 and t+8 of Figure 32.

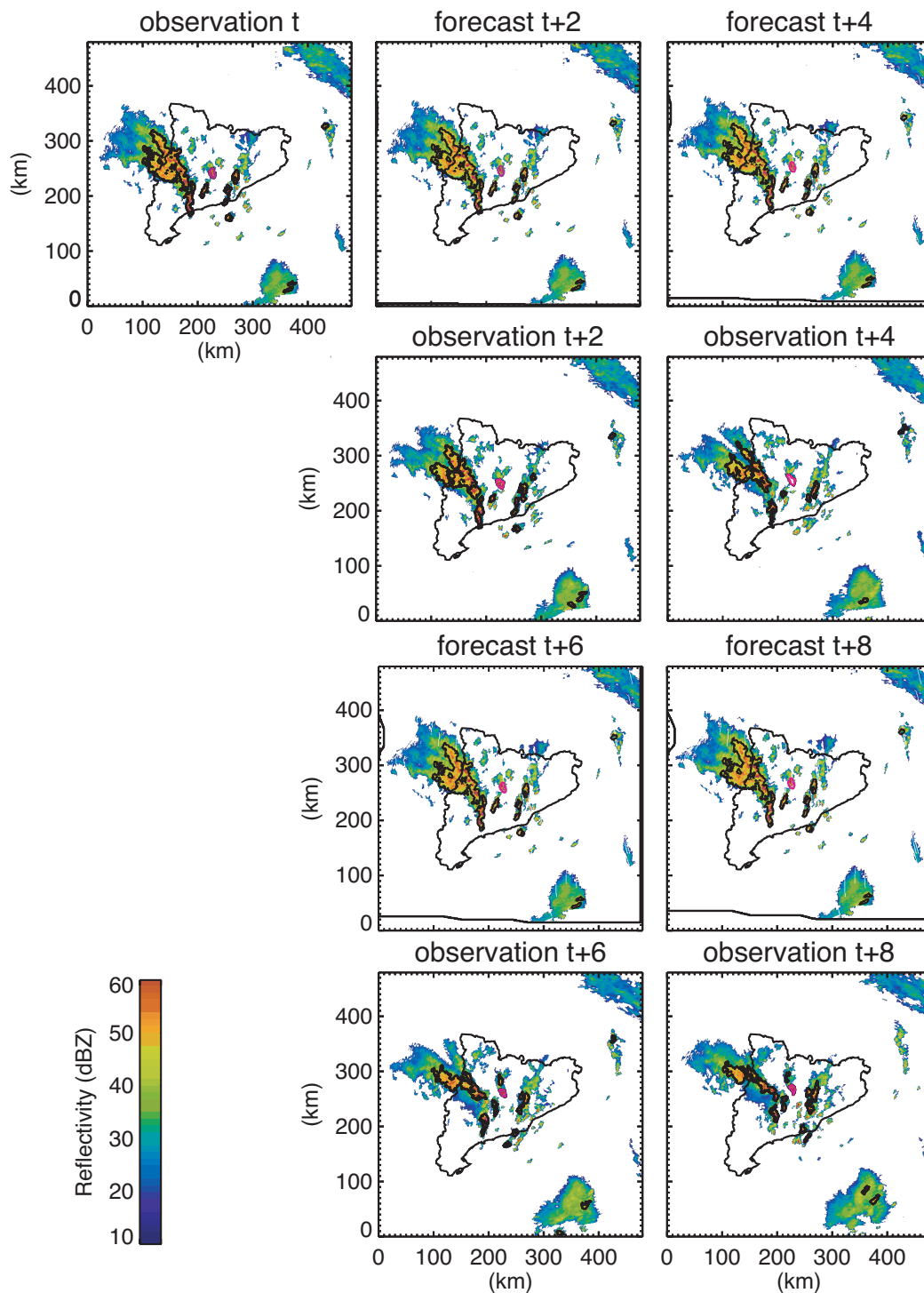


**Figure 32.** Comparison between forecasted and observed reflectivity fields. Forecasted fields were generated from observation at 12:06h UTC, for 12:18h UTC (t+2), 12:30h UTC (t+4), 12:42h UTC (t+6), and 12:54h UTC (t+8) of 15 October 2005. Below every forecasted reflectivity field the corresponding in time observed field is represented.

As in the previous case, the temporal evolution and performance of the alarms generated for this storm at two particular airports is shown in Figure 33 and Figure 34. As explained, first row represents the observation, this is when really a thunderstorm cell happened to hit the airport (in white) or not (in grey). The other rows represent the alarms set at every step of time.

In Figure 33, the temporal evolution of the alarms at airport 45 (in red in Figure 31) is represented. It can be seen in the figure that the thunderstorm was into the airport area from 12:06h UTC until 12:36h UTC (first row). From Figure 33, it is possible to see that most of the alarms generated were correctly forecasted, only that were set 6 and 12 minutes earlier (one and two steps of time) for forecasts generated from 11:12h UTC to 11:54h UTC (from second to ninth row). There were also some missed alarms, for example the alarms generated at 11:48h UTC (eighth row) didn't forecast alarms for 12:30h UTC and 12:36h UTC.

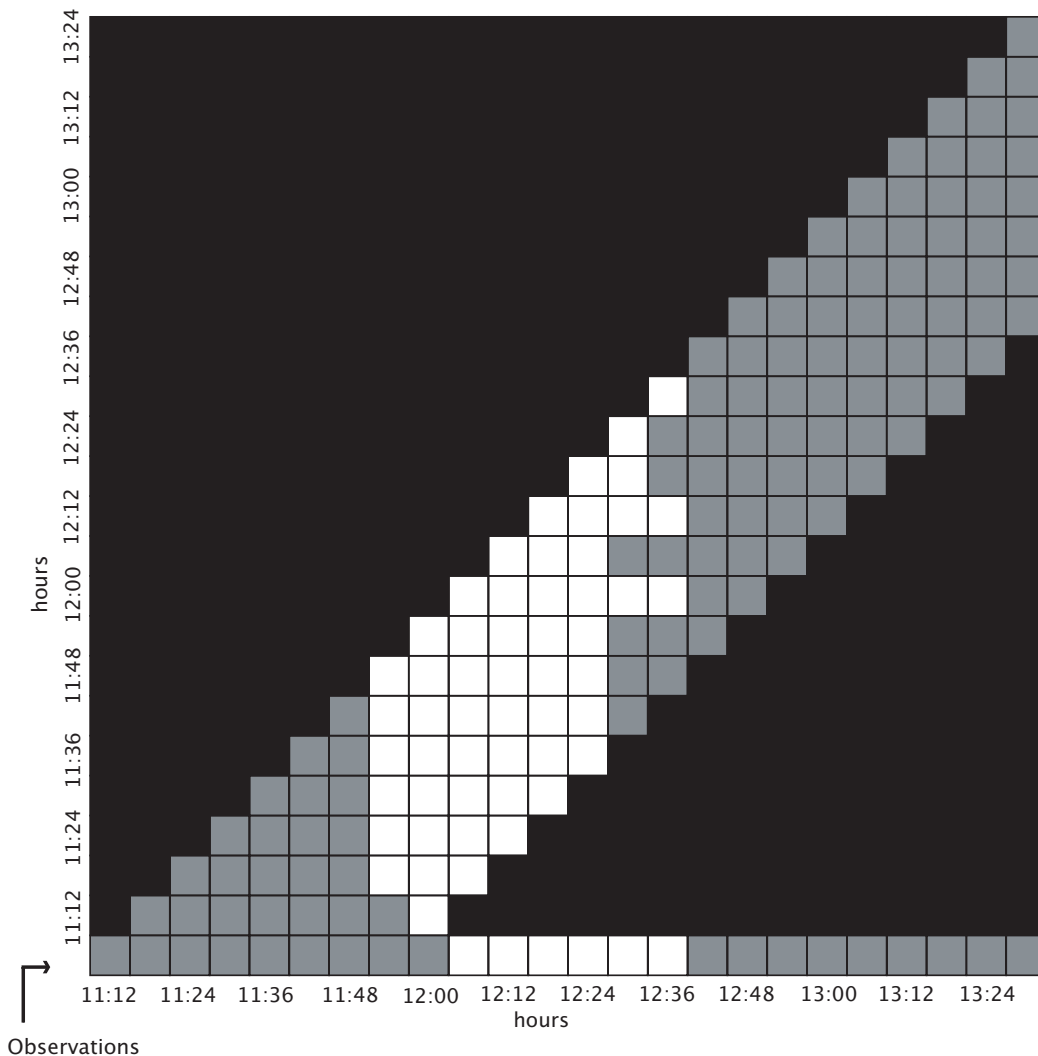


**Figure 33.** Temporal evolution of the alarms set for the specific storm studied at a specific airport (airport in red in Figure 31) from 11:12h UTC to 13:30h UTC of the 15 October 2005. The first row represents the observation at the airport. Positive cases (alarms) are represented in white, while no alarm set is represented in grey. The other rows represent steps of time for which alarms were generated.

The temporal evolution of the alarms for another airport (airport 44, in grey in Figure 31) is represented in Figure 34. Here, it is possible to observe that the thunderstorm was into the airport area from 13:00h UTC to 13:12h UTC (see first row of Figure 34). As it can be observed, it was forecasted correctly, but many false alarms were also generated.

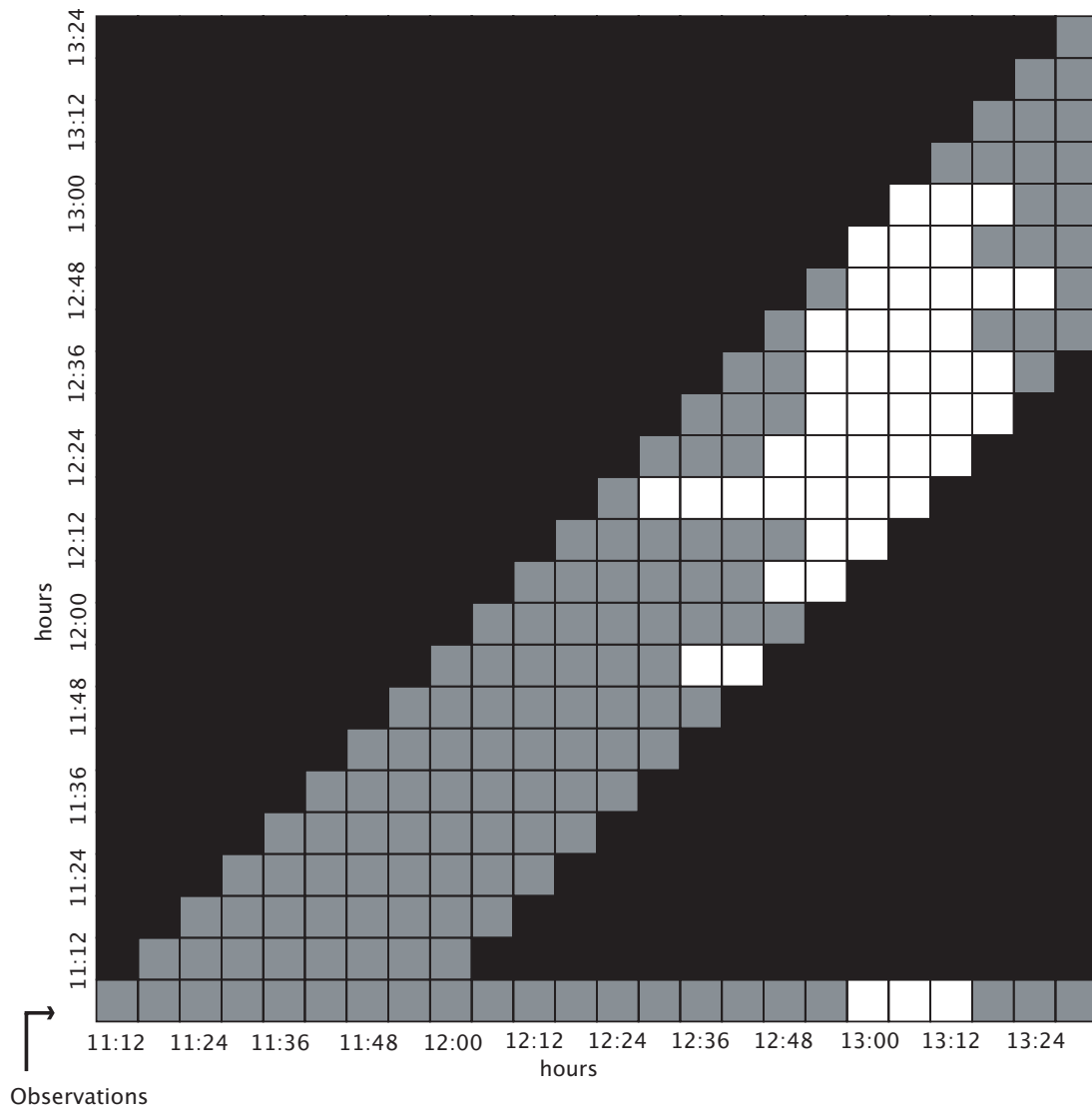


**Figure 34. Temporal evolution of the alarms set for the specific storm studied at a specific airport (airport 44, in grey in Figure 31) from 11:12h UTC to 13:30h UTC of the 15 October 2005. The first row represents the observation at the airport. Positive cases are represented in white, while no alarm set is represented in grey. The other rows represent steps of time for which alarms were generated.**

Finally, in order to statistically evaluate the behaviour of the thunderstorm nowcasting alarm system for the 15 October 2005, the mean value of the POD, FAR and CSI for all the day have been computed. They are represented in Figure 35.

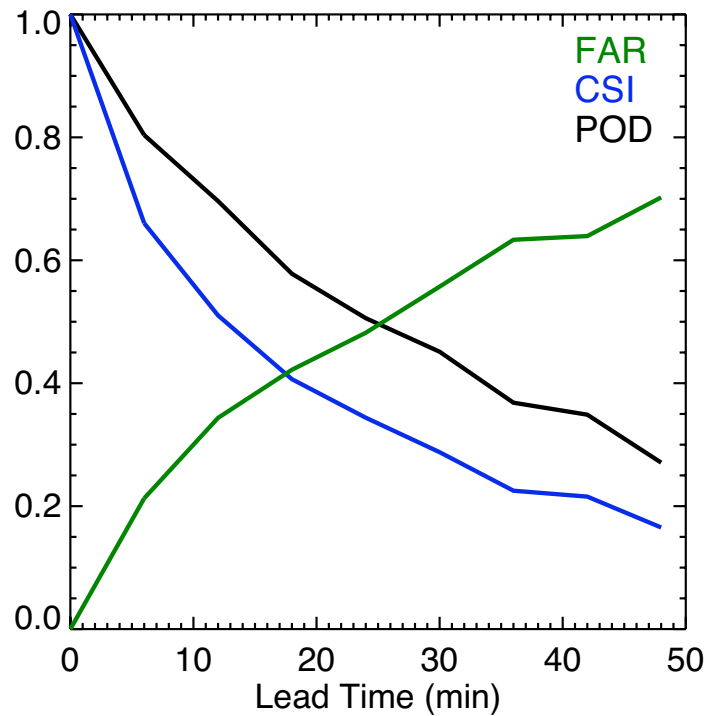


**Figure 35. Mean value of POD, FAR and CSI for the 15 October 2005.**

As seen in Figure 35, these values are pretty reliable until approximately 30 minutes of lead time. This is a satisfactory result if we take into account the short life time of the major part of the cells considered (54% of the storms lived less than 20 minutes). So POD and CSI decrease because the number of misses increases because of new cells that couldn't be forecasted with the system, and because the number of hits decreases because cells that are forecasted to continue propagating most of the time dissipate, so they don't get to hit the airport. The same thing happens with FAR, this is that the number of false alarms increases due to the same reasons.

### 4.3. Case 3: 13 September 2006

During the 13 September 2006, there were intense storm phenomena over the entire region. The general movement of the cells was from Southwest to Northeast. The horizontal extension of the storms was generally larger during the first hours of the day (see top left panel of Figure 36), while during the rest of the day they became smaller and scattered over all the territory (it can be seen in top right, bottom left, and bottom right panels of Figure 36).

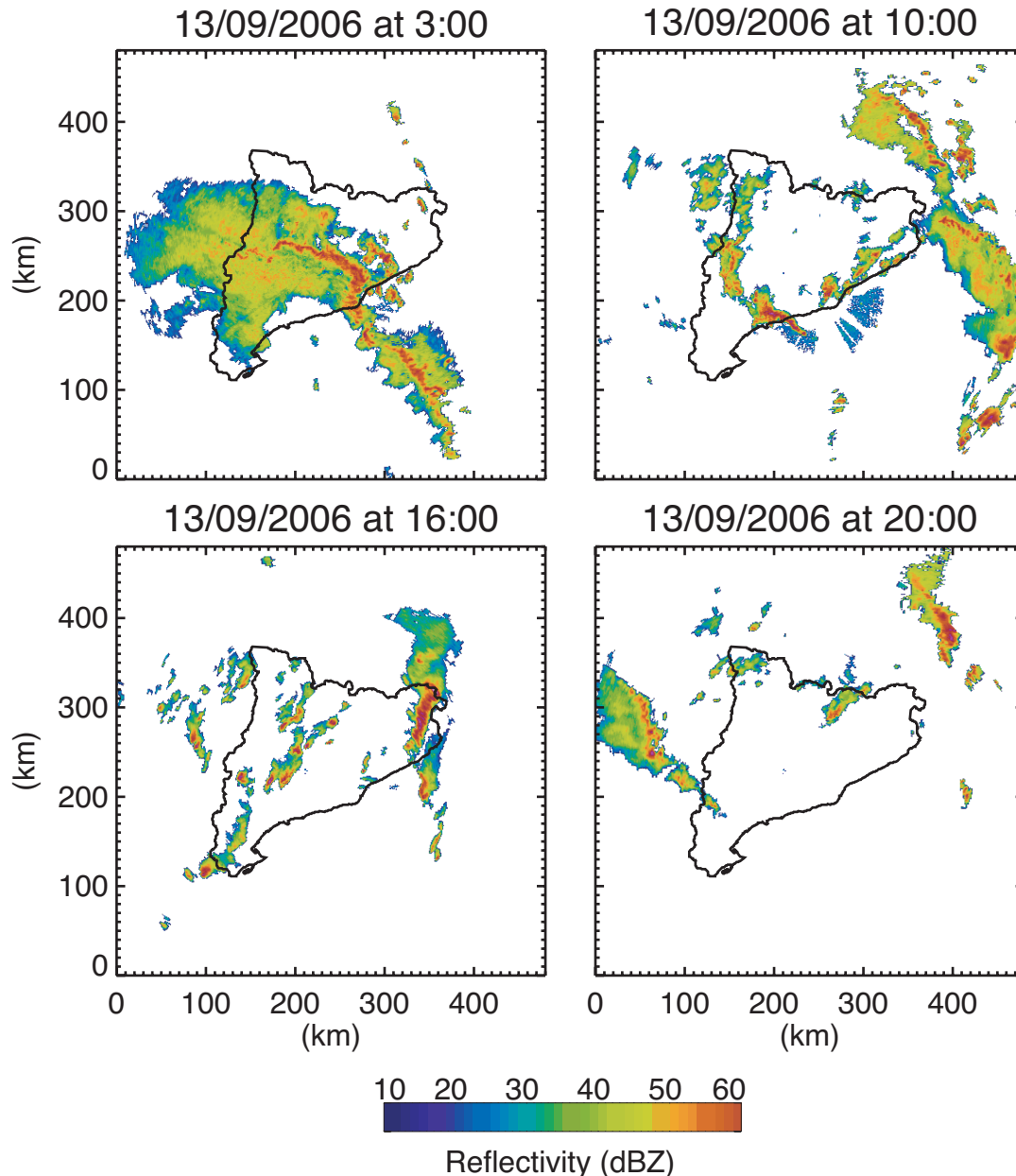


**Figure 36. Reflectivity fields observed the 13 September 2006 at 3:00h UTC, 10:00h UTC, 16:00h UTC, and 20:00h UTC.**

During the 13 September 2006, there were detected 1023 regions of intense precipitation that accomplished our definition of storm.

It has been computed that approximately 61% of these storms had life times shorter than 20 minutes. 89% of the cells lived less than 1 hour, and only 3% lived more than 2 hours. The distribution of storms depending on their time of life is represented in Figure 37a. As seen in Figure 37b, most of the cells detected during the case had mean areas of less than 500 km<sup>2</sup> (93%), but 3% were larger than 1000 km<sup>2</sup>. So, for this case of study, storms had generally very large extensions.

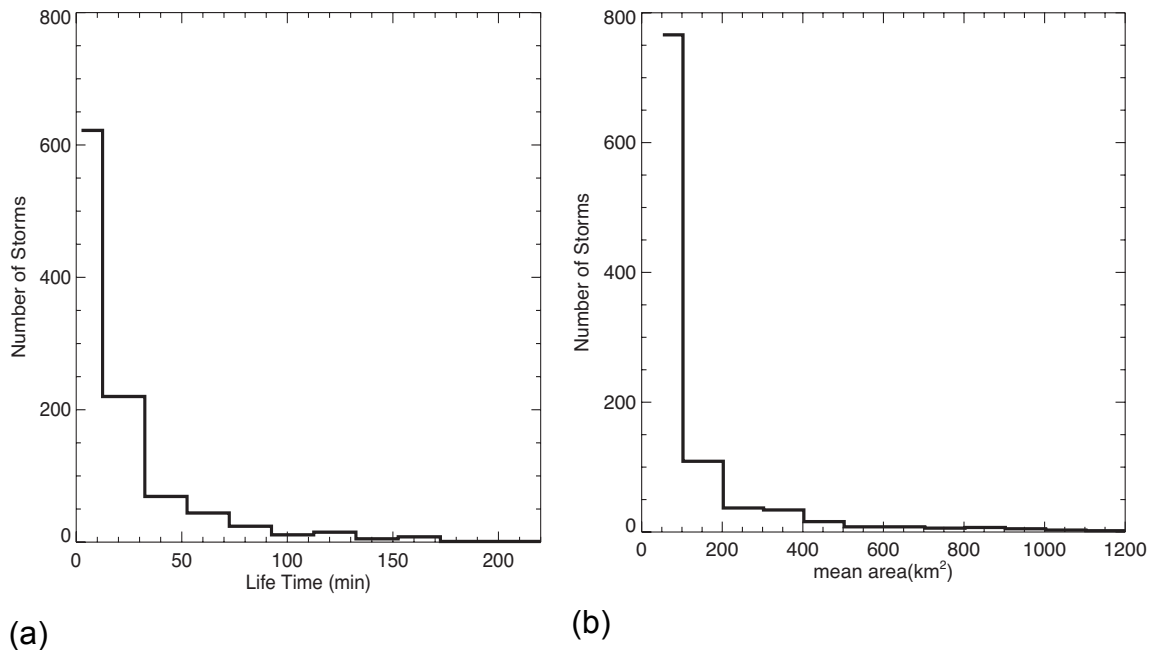


**Figure 37. (a) Number of storms in function of their life time for the 13 September 2006 (b) Number of storms in function of their mean areas for the 13 September 2006.**

In Figure 38 it is shown the relation between time of life and maximum horizontal extension reached of the storms considered in this case. It can be observed that there is an important concentration of storms on the region of the figure of small extensions (from 50 to 500 km<sup>2</sup>) and short life times (0 to 30 minutes), as it was expected. It can be seen that generally storms with bigger extensions had usually longer life duration, but it also can be observed that there are some of them that don't follow this expected relation. For example, there are storms that reached extensions between 1000 and 5000 km<sup>2</sup> with a life time inferior to 1 hour. This behaviour can be explained taking into account the way in which the algorithm handles mergers and splits. As explained in section 3.2.2.3, when a merging happens, only the history of one of the initial cells is conserved, so the other ones are supposed to die. Thus, there exist some storms that are considered to have less time of life that really had. The same way, when a split takes place, only one of the new cells inherit the history, so the time of life computed for the other ones is considered to start at the observation after the split (diminishing their real duration). These phenomena use to happen frequently when cells have large extensions.

The correlation computed for the relation life time versus maximum horizontal extension reached by the storms is 0.39. This value is not as good as the obtained in the previous two cases because of the large extension storms with short computed life times.

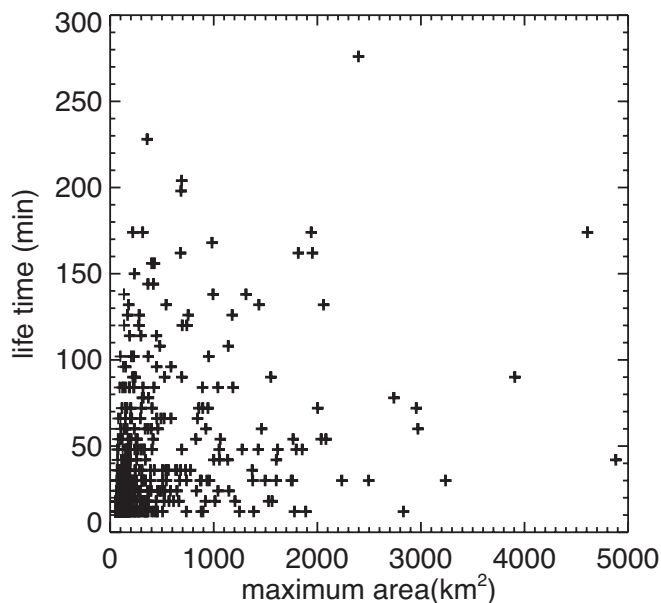


**Figure 38. Storm life time versus maximum horizontal extension of the storms detected for the 13 September 2006**

As said in the two previous cases, alarms are set at each step of time for lead times up to 48 minutes, so for a certain time it is possible to have more than one alarm if they were set at different times for different lead times. This justifies the big number of alarms set during this case: 47446 alarms.

Due to the general active convective day, there were alarms for each hypothetical airport. This also justifies the number of alarms generated this day.

As seen before, most of the storms had durations smaller than 60 minutes and an area smaller than 500 km<sup>2</sup>. So the storm chosen to study the system behaviour is a storm whose attributes are into this range of values and that lived enough to make a significative tracking. Its computed life time was 60 minutes, being detected for the first time at 17:48h UTC and for the last time at 18:48h UTC. It reached a maximum area of 527 km<sup>2</sup> and a maximum reflectivity value of 59 dBZ with a mean velocity of 11m/s. In Figure 39 the reflectivity image corresponding to the last observation where the storm was detected is represented, with the contour of the studied cell at this time represented in black. The cell track is plotted also in black, and it represents the path of the cell centroid since the storm was first detected until its death.

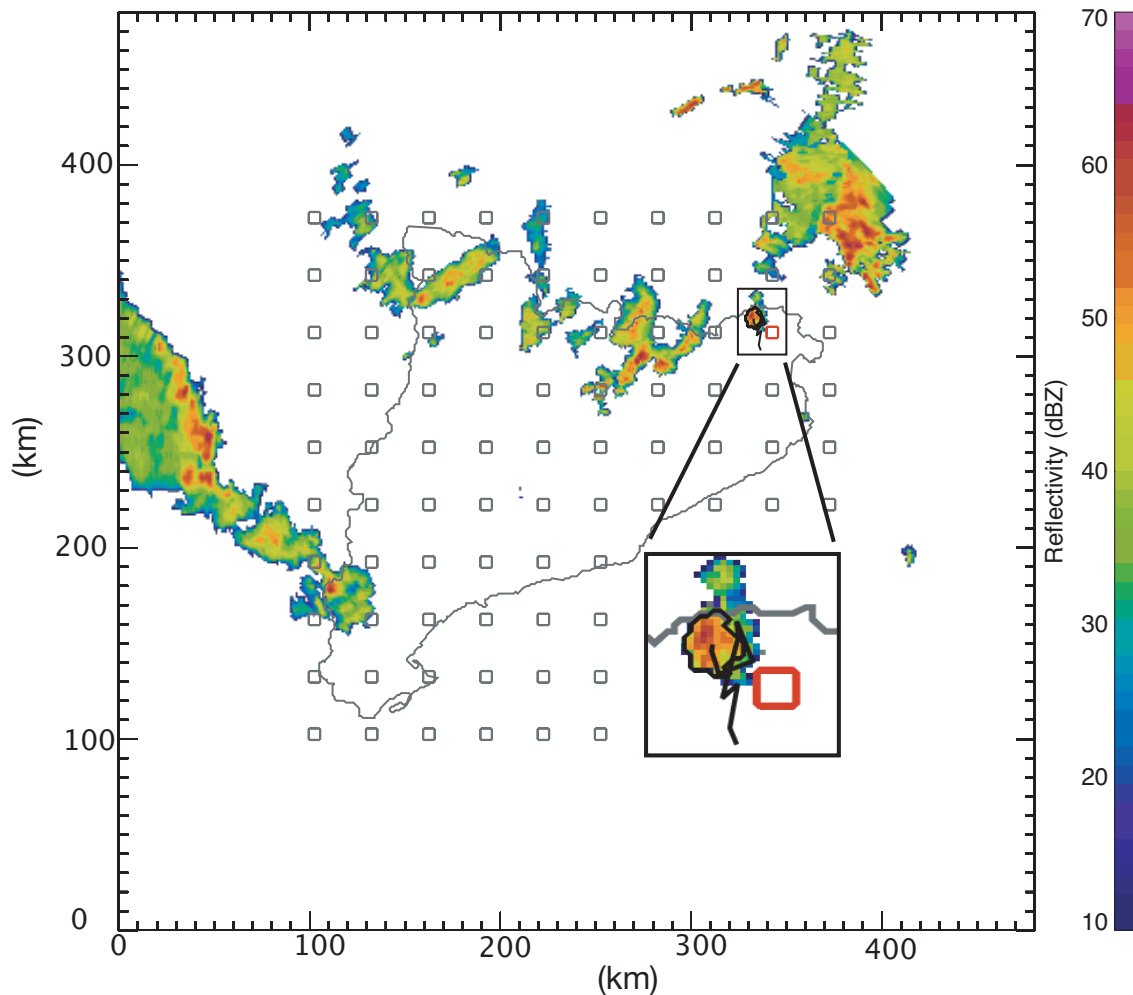


**Figure 39. Reflectivity field observed the 13 September 2006 at 18:48h UTC. The contour and track of the storm of study is represented in black.**

As it is possible to see in Figure 39, this cell only hit airport 87 (in red in the figure), but it generated false alarms at two more airports.

In Figure 39, a zoom of the area where the cell had lived is plotted. There, it is possible to observe the erratic movement of the cell centroid, and the difficulty to forecast convective cell movements.

In order to study the performance of the system forecasting storms, an example of forecast for the same storm is shown in Figure 40. Forecasts are generated from observation at 18:06h of the 13th of September of 2006 (first panel of Figure 40). Forecasts are generated for 18:18h UTC (t+2), 18:30h UTC (t+4), 18:42h UTC (t+6), and 18:54h UTC (t+8).

In Figure 40, it is possible to see that the storm of study is properly forecasted until 18:30h forecast. After that, the system kept on extrapolating its movement, but what really happened was that the storm area decayed and after that, dissipated and died.

The temporal evolution of the alarms at the airport that the storm hit is represented in Figure 41. The figure provides information about the number of hits, misses and false alarms that occurred for the studied storm at the mentioned airport. It is possible to observe that alarms were properly forecasted until 18:18h UTC and, after this time, hits and missed alarms happened.

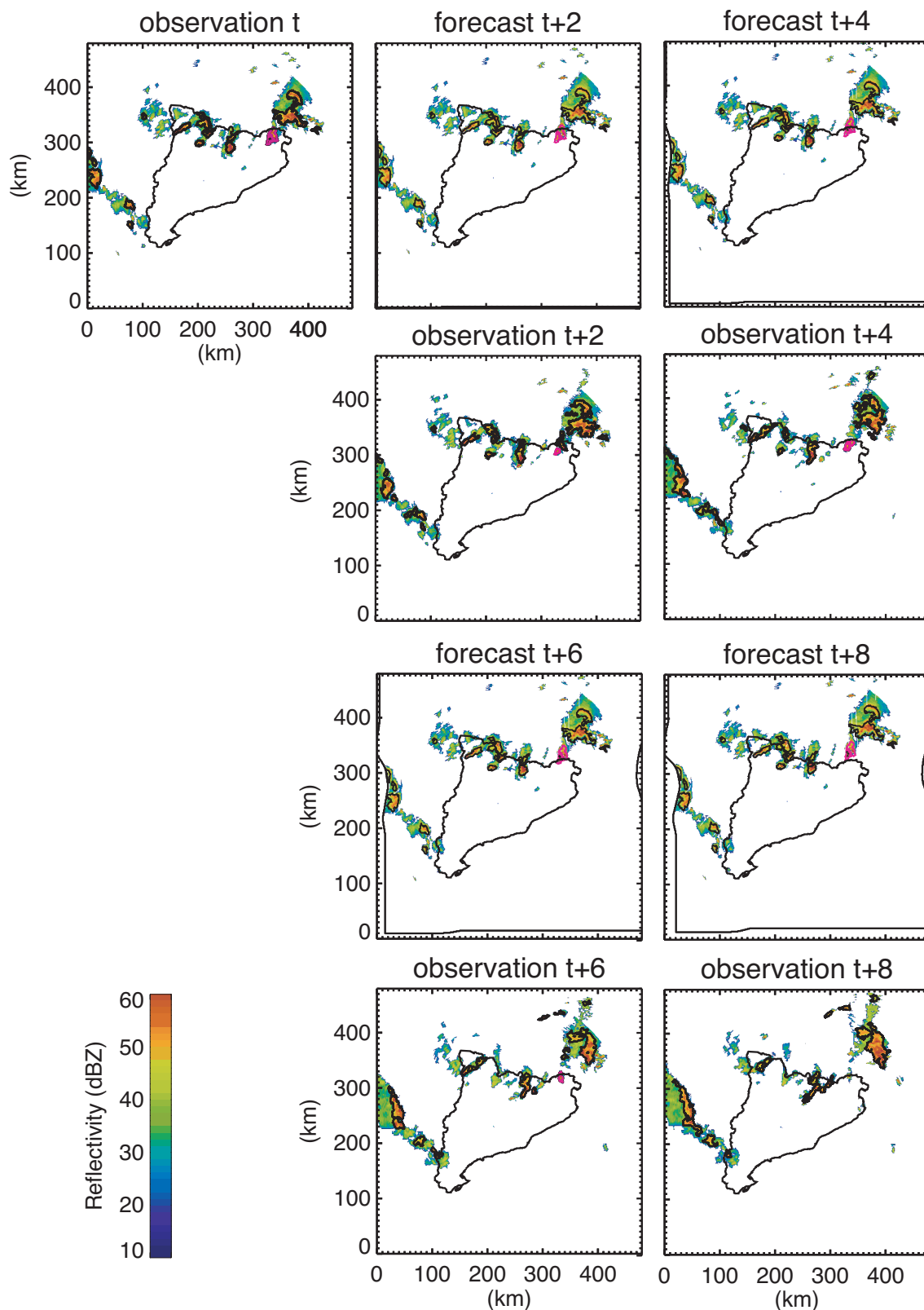


**Figure 40.** Comparison between forecasts and observations. First panel of the figure represents the reflectivity field at 18:06h UTC of the 13 September 2006 from which forecasts are generated. Forecasts represented here correspond to 18:18h UTC (t+2), 18:30h UTC (t+4), 18:42h UTC (t+6), and 18:54h UTC (t+8). Equivalent in time observed fields are represented below each forecasted field. In black there are represented the contours of the cell regions detected and forecasted, respectively. The contour of the studied storm is represented in magenta.

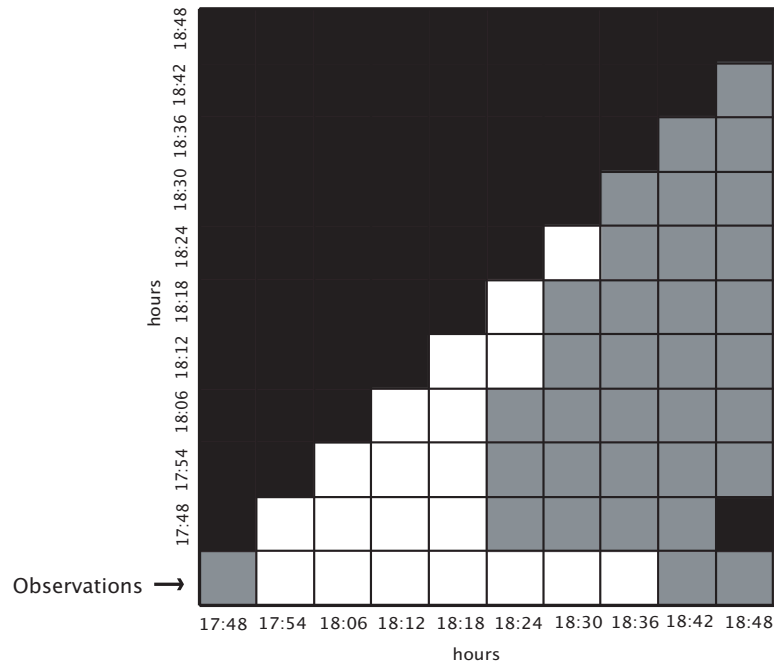


**Figure 41. Temporal evolution of the alarms set for the specific storm studied at a specific airport (airport 87, in red in Figure 41) from 17:48h UTC to 18:48h UTC of the 13 September 2006. The first row represents the observation at the airport. Positive cases are represented in white, while no alarm set is represented in grey. The other rows represent steps of time for which alarms were generated.**

The general behaviour of the system during the 13 September 2006 is studied by means of the mean value of POD, FAR and CSI. As said before, they have been computed using the missed, false alarm and hit values of all the day of study. They have been represented in Figure 42, where POD is represented in black, FAR in green and CSI in blue.

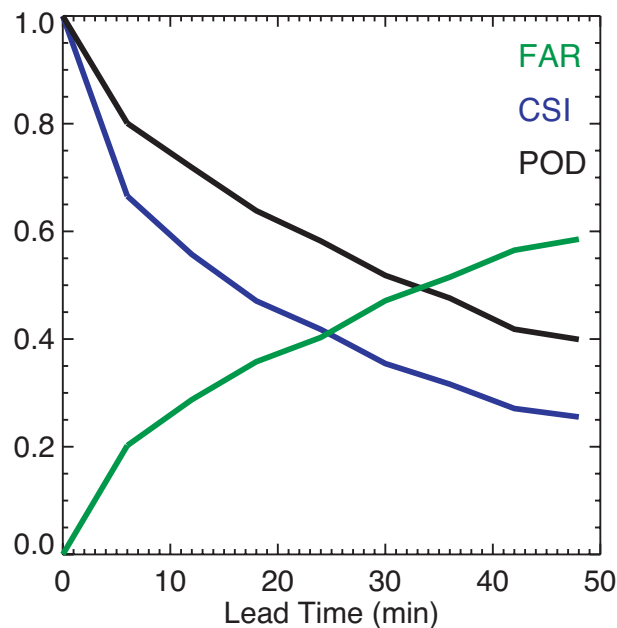


**Figure 42. Mean value of POD (in black), FAR (in green) and CSI (in blue) of the 13 October 2006.**

The present study case is the one that gives better skill score results. The reliability of the system slightly improves respect to the case of the 15 October 2005. Even so, the reliability increases only in approximately 6 minutes. But taking into account the difficulty of forecasting this kind of cells, it can be considered a good result.

## 5. CONCLUSIONS

In this Master Thesis, we have developed a nowcasting system based on radar observations oriented to thunderstorms with the purpose of providing alarms at an airport area.

The methodology followed in order to do it has been detailed in the work, and a verification of the system performance has been performed based on the statistical skill scores POD, FAR and CSI.

Three cases of active days with convective activity have been analysed in detail. A total of 1540 regions of intense precipitation defined as storms in this Master Thesis have been studied, from which approximately 60% of the storms lived less than 20 minutes and 30% had a life time between 20 and 60 minutes. This result is similar to the one obtained from a study based on data from TITAN (Wilson et al., 1998). The study showed that 83% of the storms considered had a lifetime shorter than 30 minutes, and only cells that had split or merged with other cells showed longer life times. Taking into account the results, the study concluded that forecasts greater than 20 minutes were, most of the time, not reliable.

Depending on the type of convective phenomena studied, the system performance presents different lead times of reliability. When the phenomenon is due to front boundaries (see cases analysed at section 4.2 and 4.3), the system provides better results, this is, less false alarms and a major number of alarms forecasted correctly. This can be explained by considering that in these cases cells usually move with the front, so its movement is easier to forecast. In this cases, the alarm system provides valuable information until almost 30 minutes (e.g. see 13 September 2006 case, where for 30 minutes forecast the skill scores obtained are a POD of approximately 0.55, a CSI equal to 0.35 and a FAR of almost 0.5). On the other side, when convection is due to differential heating (typical situation that cause thunderstorms during the summer months) the system provides reliable information until very short lead times. As showed in section 4.1, for the 25 June 2009 the skill scores computed for 12 minutes forecast are approximately 0.5 for the POD, 0.5 for the FAR and 0.35 for the CSI indexes. Therefore, alarms set for more than this lead time are not plenty reliable. It could be explained because this kind of storms usually have short life times and their movements not always follow a general wind movement, but a more erratic movement.

Statistical skill scores have been computed for all the studied cases together and the results show that the system could be considered reliable until approximately 30 minutes of lead time, when POD, FAR and CSI are approximately 0.5, 0.45, and 0.35 respectively. These results are represented in Figure 43.

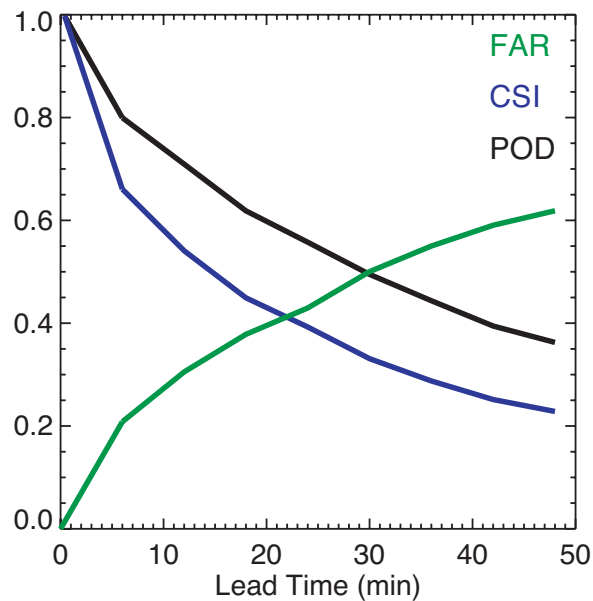


**Figure 43.** Mean values of POD (in black), FAR (in green) and CSI (in blue) for all studied cases.

The results are similar to the ones obtained in the analysis of rad-TRAM (Kober et al., 2009) where the skill scores obtained for 30 minutes of lead time are approximately 0.45 for POD, 0.55 for FAR and 0.28 for CSI. It has to be taken into account that the condition of minimum area for rad-TRAM is 30 km<sup>2</sup> and a reflectivity threshold of 37 dBZ, while in the system described here this condition is of 50 km<sup>2</sup> and 35 dBZ, so better results have to be expected for bigger areas. Results from TITAN (Dixon et al., 1993) also show similar numbers. For a lead time of 30 minutes the POD is 0.42, the FAR is 0.62 and the CSI is 0.25.

One of the mean sources of problems of the system, as said in previous chapters, is that the nowcasting algorithm used here doesn't forecast changes in shape and intensity of the cells (semi-Lagrangian persistence). So, it loses reliability rapidly because these kinds of cells have short life times, usually decaying and/or dissipating fast. This means that the number of false alarms grows considerably once reached a determined lead time (this nowcasting system works as if the cells never dissipate). Moreover, from radar observations it is not possible to detect the formation of convective cells, so they are almost always detected on their mature stage or in a stage of remaining intense precipitation. The consequence is an increase of missed alarms due to the new cells. Moreover, the movement of a convective cell not always follows the general movement on the image (wind field) due to the mechanisms that enhance them.

The system could be improved using volumetric radar data because they could allow identifying the stage of the cells. Depending on the vertical development of the cell it is possible to detect the stage and how strong the convection into the specific cell is. This is due to the fact that at stronger updrafts, the higher altitude reached and the more intense the thunderstorm is. So it would help to forecast the expected time of life of every cell, in order to diminish the number of false alarms.

A second important enhancement for the system would come from the detection of cells at their initiation stage. This could be done by means of using satellite data that provides information about the state of the atmosphere. This improvement would help to reduce the number of missed forecasts.

With the use of the data analysed in this work, a statistic could be proposed (increasing the number of studied cases) in order to forecast the time of life expected from cells depending on its features and the mechanism that formed them. This way, false alarms could be reduced (it is possible that also correctly forecasted alarms would reduce, so a detailed study would have to be done).

To summarize, the general results obtained from the study of the system show that the thunderstorm alarm nowcasting system works well for short lead times, and that this lead time of reliability, of about 30 minutes, provides some short time of reaction to the airport management, so they can try to react and take tactical decisions, as wanted on the objectives of the master thesis. However, the system developed here has to be improved and enhanced in order to provide more probability of detection, reliability and precision on the alarm generation.

## REFERENCES

- Ahrens, C. D., 2009: *Meteorology Today. An Introduction to Weather, Climate, and the Environment*. Ninth ed. Brooks/ Cole, Cengage Learning, 624 pp.
- Austin, G. L., 1985: Application of a pattern-recognition and extrapolation techniques to forecasting. *European Space Agency J.*, **9**, 147-155.
- Berenguer, M., C. Corral, R. Sánchez-Diezma, and D. Sempere-Torres, 2005: Hydrological Validation of a Radar-Based Nowcasting Technique. *Journal of Hydrometeorology*, **6**, 532-549.
- Berenguer, M., D. Sempere-Torres, C. Corral, and R. Sánchez-Diezma, 2006: A fuzzy logic technique for identifying nonprecipitating echoes in radar scans. *Journal of Atmospheric and Oceanic Technology*, **23**, 1157-1180.
- Bjerkaas, C. L. and D. E. Forsyth, 1979: Real-time automated tracking of severe thunderstorms using Doppler weather radar. *11th Conf. on Severe Local Storms, Kansas City, MO, American Meteorological Society*, 573-576.
- Carvalho, L. M. V. and C. Jones, 2001: A Satellite Method to Identify Structural Properties of Mesoscale Convective Systems Based on the Maximum Spatial Correlation Tracking Technique (MASCOTTE). *Journal of Applied Meteorology*, **40**, 1683-1701.
- Delrieu, G., J. D. Creutin, and H. Andrieu, 1995: Simulation of Radar Mountain Returns Using a Digitized Terrain Model. *Journal of Atmospheric and Oceanic Technology*, **12**, 1038-1049.
- Dixon, M. and G. Wiener, 1993: TITAN: Thunderstorm Identification, Tracking, Analysis, and Nowcasting - A Radar-based Methodology. *Journal of Atmospheric and Oceanic Technology*, **10**, 785-797.
- Duda, R. O. and R. H. Blackmer, 1972: Applications of pattern recognition techniques to digitized weather radar data. Final Rep., 135 pp.
- Evans, J. and E. Ducot, 1994: The Integrated Terminal Weather System (ITWS). *The Lincoln Laboratory Journal*, **7**, 449-474.
- Franco, M., R. Sánchez-Diezma, and D. Sempere-Torres, 2006: Improvements in weather radar rain rate estimates using a method for identifying the vertical profile of reflectivity from volume radar scans. *Meteorologische Zeitschrift*, **15**, 521-536.
- Germann, U. and I. Zawadzki, 2002: Scale-Dependence of the Predictability of Precipitation from Continental Radar Images. Part I: Description of the Methodology. *Monthly Weather Review*, **130**, 2859-2873.
- Golding, B., 1998: Nimrod, A system for generating automated very short range forecasts. *Meteorological Applications*, **5**, 1-16.
- Hering, A. M., S. Sényesi, P. Ambrosetti, and I. Bernard\_Bouissières, 2005: Nowcasting thunderstorms in complex cases using radar data. *Proceedings of The World Weather Research Programme Symposium on Nowcasting very short Range Forecasting (WSN05), Toulouse, France*.

- Hering, A. M., U. Germann, M. Boscacci, and S. S en esi, 2006: Operational thunderstorm nowcasting in the Alpine region using 3D-radar severe weather parameters and lightning data *Proceedings of the Fourth European Conference on Radar Meteorology (ERAD), Barcelona, Spain*.
- Hering, A. M., C. Morel, G. Galli, S. S en esi, P. Ambrosetti, and M. Boscacci, 2004: Nowcasting thunderstorms in the Alpine region using a radar based adaptative thresholding scheme *Proceedings of the Third European Conference on Radar Meteorology (ERAD), Visby, Sweden*, 206-211.
- Houze, R., 1993: *Cloud Dynamics*. Vol. 53, *international Geophysics Series*, Academic Press, Inc, 573 pp.
- Johnson, J. T., P. L. MacKeen, A. Witt, E. D. Mitchell, G. J. Stumpf, M. D. Eilts, and K. W. Thomas, 1998: The Storm Cell Identification and Tracking Algorithm: An Enhanced WSR-88D Algorithm. *Weather and Forecasting*, **13**, 263-276.
- Kober, K. and A. Tafferner, 2009: Tracking and nowcasting of convective cells using remote sensing data from radar and satellite. *Meteorologische Zeitschrift*, **18**, 75-84.
- Li, L., W. Schmid, and J. Joss, 1995: Nowcasting of Motion and Growth of Precipitation with Radar over a Complex Orography. *Journal of Applied Meteorology*, **34**, 1286-1300.
- Marshall, J. S. and W. M. Palmer, 1948: The distribution of raindrops with size. *Journal of Meteorology*, **5**, 165-166.
- Mecklenburg, S. A., A. Jurczyk, J. Szturc, and K. Osr odka, 2002: Quantitative precipitation forecasts (QPF) based on radar data for hydrological models. *COST Action 717: Use of radar observations in hydrological and NWP models*, 33 pp.
- Mueller, C., T. Saxen, R. Roberts, J. Wilson, T. Betancourt, S. Dettling, N. Oien, and J. Yee, 2003: NCAR Auto-Nowcast System. *Weather and Forecasting*, **18**, 545-561.
- Pierce, C. E., C. G. Collier, P. J. Hardaker, and C. M. Haggett, 2000: Gandolf: A system for generating automated nowcasts of convective precipitation. *Meteorological Applications*, **7**, 341-360.
- Pierce, C. E., E. Ebert, A. W. Seed, M. Sleigh, C. G. Collier, N. I. Fox, N. Donaldson, J. W. Wilson, R. Roberts, and C. K. Mueller, 2004: The Nowcasting of Precipitation during Sydney 2000: An Appraisal of the QPF Algorithms. *Weather and Forecasting*, **19**, 7-21.
- Reyniers, M., 2008: Quantitative Precipitation Forecasts based on radar observations: principles, algorithms and operational systems. *2008/0224/52 Koninklijk Meteorologisch Instituut van Belgi * 1-60.
- Rinehart, R. E. and E. T. Garvey, 1978: Three-dimensional storm motion detected by convective weather radar. *Nature*, 287-289.
- Rinehart, R. E., 1997: *Radar for Meteorologists*. Third ed. Rinehart Publications, 428 pp.

- Sánchez-Diezma, R., 2001: Optimización de la medida de lluvia por radar meteorológico para su aplicación hidrológica., Universitat Politècnica de Catalunya, 313 pp.
- Seed, A. W., 2003: A Dynamic and Spatial Scaling Approach to Advection Forecasting. *Journal of Applied Meteorology*, **42**, 381-388.
- Sempere-Torres, D., R. Sánchez-Diezma, M. Berenguer, R. Pascual, and I. Zawadzki, 2003: Improving radar rainfall measurement stability using mountain returns in real time. *31st International Conference on radar Meteorology*.
- Steinacker, R., M. Dorninger, F. Wölfelmaier, and T. Krennert, 2000: Automatic Tracking of convective cells and cell complexes from lightning and radar data. *Meteorology and Atmospheric Physics*, **72**, 101-110.
- Stull, R. B., 2000: *Meteorology for Scientists and Engineers*. second ed. Cengage Learning, 528 pp.
- Tsonis, A. A. and G. L. Austin, 1981: An evaluation of extrapolation techniques for the short-term prediction of rain amounts. *Atmos.-Ocean*, **19**, 54-64.
- Tuttle, J. D. and G. B. Foote, 1990: Determination of the Boundary Layer Airflow from a Single Doppler Radar. *Journal of Atmospheric and Oceanic Technology*, 218-232.
- Wallace, J. M. and P. V. Hobbs, 2006: *Atmospheric Science: An Introductory Survey*. Second ed. Vol. 92, Academic Press, 504 pp.
- Weber, M. E., M. L. Stone, and J. A. Cullen, 1993: Anomalous Propagation with Thunderstorm Outflows. *American Meteorology Society 26th Int. Conf. on Radar Meteorology, Norman, OK*, 238-240.
- Wilk, K. E. and K. C. Gray, 1970: Processing and analysis techniques used with the NSSL weather radar system. *14th Radar Meteorology Conf.*, 369-374.
- Wilson, J. W., N. A. Crook, C. K. Mueller, J. Sun, and M. Dixon, 1998: Nowcasting Thunderstorms: A Status Report. *Bulletin of the American Meteorological Society*, **79**, 2079-2099.
- Zinner, T., H. Mannstein, and A. Tafferfer, 2008: Cb-TRAM: Tracking and Monitoring severe convection from onset over rapid development to mature phase using multi-channel Meteosat-8 SEVIRI data. *Meteorology and Atmospheric Physics*, **101**, 191-210.
- Zittel, W. D., 1976: Computer applications and techniques for storm tracking and warning. *17th Conf. on Radar Meteorology*, 514-521.